DISSERTATION

ALTERNATIVE HEART ASSISTANCE PUMP

Submitted by

Alireza Sharifi

Department of Mechanical Engineering

In partial fulfillment of the requirements

For the Degree of Doctor of Philosophy

Colorado State University

Fort Collins, Colorado

Spring 2021

Doctoral committee:

Advisor: David Bark
Co-Advisor: Susan James

Xinfeng Gao
Ketul Popat
Brian Scansen

ABSTRACT

ALTERNATIVE HEART ASSISTANCE PUMP

On average, the human heart beats around 115,000, and pumps around 2,000 gallons of blood daily. This essential organ may undergo systolic or diastolic dysfunction in which the heart cannot properly contract or relax, respectively. To help hearts pump effectively should these types of failures occur, ventricular assist devices (VAD) are implemented as a temporary or permanent solution. The most common VAD is the left ventricular assist device (LVAD) which supports the left ventricle in pumping the oxygen-rich blood from the heart to the aorta, and ultimately to the rest of the body. Although current VADs are an important treatment for advanced heart failure, generally VADS come with many complications and issues after implantation. These complications include incidents of hemolysis (tearing of the blood cells), thrombosis (clotting of the blood), bleeding (especially in the gastrointestinal tract), and infection at the driveline site. Specifically, the current continuous flow pumps are associated with a much higher incidence of gastrointestinal bleeding, myocardial perfusion, kidney problems, among others, compared with the earlier generation pulsatile pumps. However, the presence of several moving mechanical components made the pulsatile pumps less durable, bulky, and prone to malfunction, ultimately leading to favor toward continuous flow designs.

The goal of the present study is to develop a novel heart assist pump, overcoming drawbacks to current commercially available pumps, by improving hemodynamic (blood flow) performance, pulsatility, and eliminating bleeding disorders. Our design will overcome the current pumps which suffer from non-physiological flow, and blood damage. The impact of this work goes beyond heart assist devices and would be applicable to other blood pumps.

The fundamental biological and physical principles of designing a blood pump will be reviewed in chapter one. In addition, recent studies on current LVADs and the motivation behind these studies will also be discussed. Then, the idea of using a contractive tubular heart as an alternative pump will be presented in chapter two. To understand the pumping mechanism of the tubular heart, a detailed study on the embryonic heart is presented in this chapter.

Subsequently, the effect of flow forces on blood cells will be studied in chapter 3. Moreover, the relation between flow regime and bleeding disorders have been studied in the same chapter. A discussion of our design, including the pump design, testing set up, experimental results will be presented in chapter 4. Finally, the limitations of the present study and future work will be presented in chapter 5.

ACKNOWLEDGEMENTS

I would like to acknowledge my indebtedness and render my warmest thanks to my advisor Dr. David Bark. He is always happy and willing to help me solve the confusions and direct me approach to the final result of the thesis. Without his encouragement and support, I would not finish my PhD study.

Furthermore, I would like to appreciate my co-advisor, Dr. James who have helped me undertake this research. Many thanks to my PhD committee members, Dr. Gao, Dr. Popat and Dr. Scansen for extended discussions and valuable suggestions which have contributed greatly to the improvement of the thesis. I must express my gratitude to Dr. Bortot and Dr. Di Paola who helped we to have a better understanding of the biology side of my PhD work.

I would also like to say a heartfelt thank you to my family for always believing in me and encouraging me to follow my dreams. They have sacrificed for bringing me up and providing me in every possible way.

Finally, I would like to thank the Mechanical engineering department, and specially Dr. Petro for the GTA opportunity which introduced me to several interesting senior design projects.

TABLE OF CONTENTS

LIST OF TABLES

LIST OF FIGURES

CHAPTER 1: HEART ASSISTANT PUMPS BACKGROUND

1.1. INTRODUCTION

Cardiovascular disease has remained the leading cause of death for over a century in the United States [1,2]. One result has been an increasing number of ventricular assist devices (VAD)s being utilized to treat patients with various forms of heart failure, affecting 23 million people worldwide [3,4]. There are 4 classes of the heart failure which are mostly defined by patient ability to do physical activities. Ejection fraction refers to the amount of blood being pumped out of the left ventricle each time it contracts, can be used to quantify severity of heart failure. In the first class of heart failure there is no limitation of physical activity. In the second class of heart failure there is slight limitation of physical activity and the patient has significant limitation in physical activities in the third class. The patient in the fourth stage of heart failure is unable to carry on any physical activity without discomfort and the ejection [5]. The ejection fraction varies for the patients with heart failure. Patient with ejection fraction smaller than 20% and systolic blood pressure <80 mmHg needs a heart transplant, which is the primary solution for many of these patients [6]. However, fewer than 3820 heart transplants are performed in the world each year due to an insufficient number of available viable hearts, despite a much larger need [7,8]. Due to the need for an alternative, VADs were developed as mechanical pumps that enhance or replace the function of the ventricle. Continuous-flow VADs are the most commonly used and consist of a driveline connected through the skin of a patient to control a mechanical impeller rotating inside a housing to pump blood (Fig.1.1). Despite substantial improvements in VADs (especially durability), a larger application of the technology has been limited due to clinically significant adverse events that include bleeding and thrombosis issues [6,9–13].

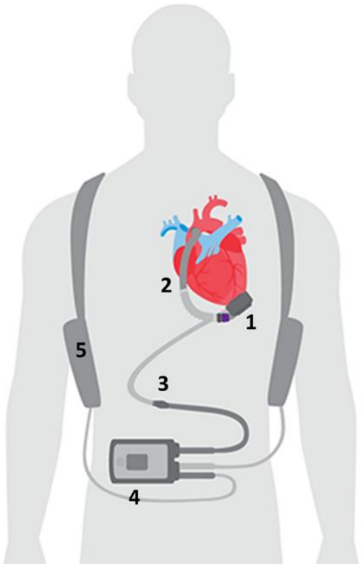

Figure 1.1. The LVAD parts, 1: pump, 2: outflow cannula, 3: driveline, 4: controller, 5: batteries

1.2. LEFT VENTRICULAR ASSIST DEVICE HISTORY

To begin, there are three generations of the left ventricular assist devices. The first generation was the initial development of ventricular assist devices. This primary development was initiated after the concepts of the total artificial heart were not successful [12]. For example, the JARVIK-7 TAH, the world's first permanent artificial heart, was implanted into the body of Dr. Barney Clark on December 2, 1982. Although this was a revolutionary device made of aluminum and polyurethane, the device supported the patient for only 112 days [14]. Furthermore, the amount of total artificial hearts in mechanical assist devices is under 1% [10]. The VADs were electrically or pneumatically driven membrane pumps. They created pulsatile flow while incorporating artificial heart valves for the inlet and outlet. The pumps were connected to the cannulas of the heart serving as a left, right, or biventricular device. It is important to note that the first-generation systems were designed solely for bridge to transplant therapy. Because these were the first-generation systems, there were some disadvantageous aspects of these devices that included more noise produced, high infection rate of the cannulas, malfunctions created by tears in the membrane, large sizes of the devices, and deterioration of the heart valves. The most significant systems conceived in the first generation were the Berlin Heart EXCOR, Thoratec PVAD, and Thoratec XVE [12]. There were some disadvantageous aspects of these devices such as infections around the areas of cannula implantation [13]; poor eating habits due to stomach compression that resulted from having the LVAD [15]; thrombosis and bleeding was also reported among patients [16]. Thirdly, they are also prone to mechanical malfunctioning due to deterioration of the parts of LVAD such as the membrane or the valves; these could sometimes lead to fatal complications [12].

The second generation of devices progressed in the 1990's. Improvements to the size, susceptibility to infection, and reduction in noise improved the patients' quality of life. These devices were purely used as LVADs rather than BIVADs and LVADs. The most significant device created during this generation was the HeartMate II.

Unlike the first generation VADs, the HeartMate II LVAD is an axial-flow rotary VAD with a blood pump, percutaneous lead, external power source, and system driver. This pump, specifically a univentricular device, is implanted between the left ventricle and the ascending aorta and is designed for long term use [17]. The system can create flow rates up to 10 L per minute. The device works in a fixed speed mode, so it does not automatically vary depending on the blood flow of the individual. Material wise, the internal surfaces including the rotor, inlet stator, outlet stator, and thin-walled duct are smooth polished titanium. A textured titanium microsphere surface covers the sealed inflow conduit and outflow elbow [18]. When the system was introduced to the public and used in heart failure patients, studies showed that there was a significantly lower postoperative mortality rate and lower incidence of adverse events. At the time, the device as a whole was smaller than previous VADs and reduced postoperative bleeding and infection rate. There were issues and negatives to the device. Patients using the device required anticoagulation therapy; there were concerns about loading and unloading of the left ventricle; and, most significantly, there were increased incidents with gastrointestinal (GI) bleeding in patients [19].

The third generation of LVADs were even smaller in size. During this generation, several devices rose to prominence including the HeartWare LVAD and HeartMate 3. These systems utilized the centrifugal continuous flow design. They have been engineered for even longer durability (5 to 10 years), a more compact shape, easier surgical placement, and lower rates of hemolysis and thrombosis [12].

A study performed in 2017, two years after the HeartMate 3 received its CE mark, showed the effectiveness of the device six months after implantation. According to the study, the 6-month survival after the implantation was about 85.2% while showing 0% stroke, and 0% pump thrombosis rates after six months [20]. According to a separate study that followed 44 patients with the HeartMate 3 for two years, 80% of the patients were readmitted at least one time over the two-year study. Over the two-year time period, there were a total of 104 readmissions from the 80% of patients. About 79% of the 104 readmission events were for adverse events. Bleeding and infection were the two major adverse events [21].

HeartWare, DuraHeart and HeartMate III are emerging devices based on these principles. Although clinical experience with these pumps are just getting under way, early results show improvement in patients' health [13,17,18,21]. The most recent studies show that Heartmate 3 is still suffering from pump thrombosis, GI bleeding and driveline infection [22].

1.2.1 IMPLANTED LVAD CHARACTRISTICS

The pump inlet is inserted into the apex of the left ventricle, and the outflow cannula, connected to the pump, is anastomosed to the ascending aorta. Oxygen enriched blood returns from the lungs to the left side of the heart and exits through the left ventricular apex to the pump. Blood is then actively pumped into the ascending aorta. The pumping chamber is placed within the abdominal wall or peritoneal cavity. A percutaneous drive line carries the electrical cable to the battery packs and electronic controls, which are worn on a shoulder holster and belt, respectively.

1.2.2 LVAD CURRENT PROBLEMS

Clinical observations showed that the continuous flow pumps (second and third generations) are associated with a much higher incidence of gastrointestinal bleeding (the incidence is around 40%) compared with the earlier pulsatile LVADs where the incidence was ≈10%), and patients are 4.5 to 10 times more likely to experience gastrointestinal bleeding depending on the series. Moreover, continuous, non-pulsatile flow of blood through the vasculature differs from the normal physiologic state, with significant pathophysiologic implications. Moreover, the reduced pulsatility produced by a continuous flow LVAD implantation induced severe periarteritis in the kidneys and remodeling of vasculature [23]. Therefore, it is important to look into the pulsatility timing that could be used in any pulsatile device such as LVADs.

Nonsurgical bleeding, especially in the gastrointestinal tract, is one of the most common complications with patients receiving VAD. Clinicians balance the anticoagulant therapy to prevent thromboembolic events without promoting bleeding [24–26]. High non-physiological shear stress and reduced pulse pressure may be involved in increased bleeding_risk [27]. Fast impeller rotation causes large amount of shear. Some regions of flow experience a shear stress >50

Pa and can even exceed 150 Pa [28,29]. Comparatively, the highest physiological shear stress is 12 Pa. High shear stress can lead to acquired von Willebrand Syndrome (aVWS) – a loss of high molecular weight von Willebrand Factor (VWF) multimers, which occurred in all patients receiving left VADs in at least one study [19,30]. Reduction in platelet aggregation for patients with a continuous flow VAD is another adverse effect of high shear stress [19,31]. As opposed to directly effecting the cells and proteins involved in hemostasis, lack of pulse pressure in these VADs, specifically, can lead to arterial remodeling in response to altered mechanical stress [26,32]. Overall, the mechanism for bleeding can be multifactorial and remains unclear, yet what is clear is that non-physiological shear stress in VADs, potentially combined with continuous flow leads to bleeding complications [19,26,29–31]. Approximately 40% to 50% of VADs patients have some form of infection, and the associated mortality is approximately 50%. Infection is the leading cause of death for VADs patients with end-stage heart failure. Although in commercially available VADs the pumping chambers are implanted in subcutaneous, pre-peritoneal, or intra-peritoneal positions, they are connected via cables to electrical power and control packs. The exit sites through the skin for these connections have been a known source of infection. By following percutaneous tubes into the subcutaneous tissues, infections can appear and may then continue to the pump site, resulting to chronic infection. This may lead to infection of the implanted parts and possibly sepsis. This problem will be solved if all the parts of the VADs machine are implanted inside the body which is not possible with the current VADs. This problem will be solved with our fully implantable heart assistant sleeve.

In addition to infection, thromboembolic complications are another major concern for VADs. Thrombus formation is highly related to the blood-material surface interactions and hemodynamics [33]. It occurs as an undesired hemostatic response. High shear stress and shear gradients are reported to promote rapid thrombus growth, along with hemolysis and VWF self-association [33–39]. VWF is a key protein for platelet capture at high shear stress. Although recent advances in continuous flow pumps have increased the probability of survival, the number of patients experiencing device thrombosis or ischemic stroke remain high for continuous flow VADs [40,41].

1.2.3 LVAD STATE OF ART

Although the current VADs are helping patients, developing new VADs is a hot trend in the medical device field. Soft robotics can be used to create implantable sleeves that are able to provide circulatory support for patients with heart failure. By using soft robotics as circulatory support, cardiac function can be closely replicated rather than disrupted from something such as a continuous flow pump [42]. These sleeves are also non-blood contacting which gives it an advantage over traditional VADs as there is no longer the risk of hemolysis from the pump itself. The heart achieves its complex motion through the muscle layers being arranged both helically and circumferentially. There is a transcutaneous drive line for power which increased the risk of infection. The biggest complication with these sleeves is injuring and deforming the heart tissues and increase the risk of infection. This design is not commercially available.

The other invention is the C-Pulse system, a treatment option under study, designed for patients with moderate to severe heart failure in order to assist the heart to pump blood rather than replace the heart function like VADs do, and it is also designed to be disconnected for short periods of time for any number of possible reasons [43]. The C-Pulse is a system that consists of a polyurethane balloon and polyester wrap that is fitted around the aorta. The balloon is a counterpulsation device as it deflates prior to systole, thus reducing afterload, and it reinflates during diastole in order to increase blood flow to the coronary arteries [44]. This device has not been successful to help patients with severe heart failure. The effect of the contracting the aorta on its structure is still unknown. The device is also pneumatic and there is drive line infection risk like any other heart assistant device.

Corwave LVAD is another new developed LVAD. It is designed to deliver gentle oscillation of a membrane to propel blood based on the wave motion of a swimming fish [44], and this device still utilizes a transcutaneous drive line for power. This LVAD has been tested in both blood analogues and actual blood in flow loops, as well as being implanted in a total of 25 sheep. The results of the tests showed the pump can reliably produce over 6 L/min of blood flow (average of 5-6 L/min [45]) with maximum shear rates that are lower than those found in LVADs that use rotary pumps. As this system is not fully implantable, the infection risk is still high. As the first human implant is going to be in 2020, there is not enough data related to the device complications.

1.3 CONCLUSION

Although mechanical circulatory support saved many lives during the last decade, clinical observations have shown that the continuous flow pumps are associated with a much higher incidence of gastrointestinal bleeding, myocardial perfusion, kidney problems, among others, compared with the earlier generation pulsatile pumps. Therefore, designing a pump which can produce the sufficient pulsatile flow and pressure can be a significant step toward heart assist devices development. The zebrafish embryonic tubular heart provides enough flow and pressure without causing any complications. Therefore, we have studied the pumping mechanism in tubular stages in chapter 2. To have a better understanding of the bleeding complications, we have studied the effects of the flow mechanical forces on bleeding disorders in chapter 3. Our findings provide a new insight in VWF cleavage and consequently bleeding disorders.

In an attempt to take the best features of continuous and pulsatile pumps, we created a pump that can fully supplement a failing heart. The pump has been tested in a left heart simulator system and the results are presented in chapter 4. Finally, in chapter 5 we discuss the overall conclusion/summary for all chapters and discusses future directions.

1.4 REFERNCES:

1. Englert, J.A.; Davis, J.A.; Krim, S.R. Mechanical Circulatory Support for the Failing Heart: Continuous-Flow Left Ventricular Assist Devices. *Ochsner Journal* **2016**, *16*, 263–269.
2. Reddy, K.S. Global Perspective on Cardiovascular Disease. *Evidence-Based Cardiology* **2003**, *91102*.
3. Shaffer, F.; McCraty, R.; Zerr, C.L. A Healthy Heart Is Not a Metronome: An Integrative Review of the Heart's Anatomy and Heart Rate Variability. *Frontiers in psychology* **2014**, *5*, 1040.
4. Clawson, B.J. Incidence of Types of Heart Disease among 30,265 Autopsies, with Special Reference to Age and Sex. *American Heart Journal* **1941**, *22*, 607–624.
5. Caraballo, C.; Desai, N.R.; Mulder, H.; Alhanti, B.; Wilson, F.P.; Fiuzat, M.; Felker, G.M.; Piña, I.L.; O'Connor, C.M.; Lindenfeld, J. Clinical Implications of the New York Heart Association Classification. *Journal of the American Heart Association* **2019**, *8*, e014240.
6. Lund, L.H.; Matthews, J.; Aaronson, K. Patient Selection for Left Ventricular Assist Devices. *European journal of heart failure* **2010**, *12*, 434–443.
7. Flaherty, M.P.; Moses, J.W.; Westenfeld, R.; Palacios, I.; O'Neill, W.W.; Schreiber, T.L.; Lim, M.J.; Kaki, A.; Ghiu, I.; Mehran, R. Impella Support and Acute Kidney Injury during High-Risk Percutaneous Coronary Intervention: The Global CVAD Renal Protection Study. *Catheterization and Cardiovascular Interventions* **2020**, *95*, 1111–1121.
8. Kannel, W.B. Hazards, Risks, and Threats of Heart Disease from the Early Stages to Symptomatic Coronary Heart Disease and Cardiac Failure. *Cardiovascular drugs and therapy* **1997**, *11*, 199–212.
9. Azevedo, A.; Bettencourt, P.; Alvelos, M.; Martins, E.; Abreu-Lima, C.; Hense, H.-W.; Barros, H. Health-Related Quality of Life and Stages of Heart Failure. *International journal of cardiology* **2008**, *129*, 238–244.
10. Lund, L.H.; Khush, K.K.; Cherikh, W.S.; Goldfarb, S.; Kucheryavaya, A.Y.; Levvey, B.J.; Meiser, B.; Rossano, J.W.; Chambers, D.C.; Yusen, R.D. The Registry of the International Society for Heart and Lung Transplantation: Thirty-Fourth Adult Heart Transplantation Report—2017; Focus Theme: Allograft Ischemic Time. *The Journal of Heart and Lung Transplantation* **2017**, *36*, 1037–1046.
11. Jhun, C.-S.; Reibson, J.D.; Cysyk, J.P. Effective Ventricular Unloading by Left Ventricular Assist Device Varies with Stage of Heart Failure: Cardiac Simulator Study. *Asaio Journal* **2011**, *57*, 407–413.
12. Prinzing, A.; Herold, U.; Berkefeld, A.; Krane, M.; Lange, R.; Voss, B. Left Ventricular Assist Devices—Current State and Perspectives. *Journal of thoracic disease* **2016**, *8*, E660.
13. Sousa Casasnovas, I.; Díez Villanueva, P.; Díez del Hoyo, F.; Ruiz Fernández, M.; González Pinto, Á.; Fernández-Avilés, F. Two Different Sites of Membrane Rupture in the Berlin-Heart EXCOR Ventricular Assist Device. *Revista Española de Cardiología* **2016**, *69*, 525–527.
14. DeVries, W.C.; Anderson, J.L.; Joyce, L.D.; Anderson, F.L.; Hammond, E.H.; Jarvik, R.K.; Kolff, W.J. Clinical Use of the Total Artificial Heart. *New England Journal of Medicine* **1984**, *310*, 273–278.
15. Association, A.H. The Past, Present and Future of the Device Keeping Alive Carew Thousands of HF Patients. *American heart association news* **2016**.

16. Rodriguez, L.E.; Suarez, E.E.; Loebe, M.; Bruckner, B.A. Ventricular Assist Devices (VAD) Therapy: New Technology, New Hope? *Methodist DeBakey cardiovascular journal* **2013**, *9*, 32.
17. Griffith, B.P.; Kormos, R.L.; Borovetz, H.S.; Litwak, K.; Antaki, J.F.; Poirier, V.L.; Butler, K.C. HeartMate II Left Ventricular Assist System: From Concept to First Clinical Use. *The Annals of thoracic surgery* **2001**, *71*, S116–S120.
18. Maltais, S.; Kilic, A.; Nathan, S.; Keebler, M.; Emani, S.; Ransom, J.; Katz, J.N.; Sheridan, B.; Brieke, A.; Egnaczyk, G. PREVENtion of HeartMate II Pump Thrombosis through Clinical Management: The PREVENT Multi-Center Study. *The Journal of Heart and Lung Transplantation* **2017**, *36*, 1–12.
19. Muthiah, K.; Connor, D.; Ly, K.; Gardiner, E.E.; Andrews, R.K.; Qiao, J.; Rutgers, D.; Robson, D.; Low, J.; Jarvis, S. Longitudinal Changes in Hemostatic Parameters and Reduced Pulsatility Contribute to Non-Surgical Bleeding in Patients with Centrifugal Continuous-Flow Left Ventricular Assist Devices. *The Journal of Heart and Lung Transplantation* **2016**, *35*, 743–751.
20. Hanke, J.S.; Dogan, G.; Rojas, S.V.; Zoch, A.; Feldmann, C.; Deniz, E.; Avsar, M.; Warnecke, G.; Haverich, A.; Schmitto, J.D. First Experiences with HeartMate 3 Follow-up and Adverse Events. *The Journal of thoracic and cardiovascular surgery* **2017**, *154*, 173–178.
21. Schmitto, J.D.; Pya, Y.; Zimpfer, D.; Krabatsch, T.; Garbade, J.; Rao, V.; Morshuis, M.; Beyersdorf, F.; Marasco, S.; Sood, P. Long-Term Evaluation of a Fully Magnetically Levitated Circulatory Support Device for Advanced Heart Failure—Two-Year Results from the HeartMate 3 CE Mark Study. *European journal of heart failure* **2019**, *21*, 90–97.
22. Banfi, C.; Rigamonti, F.; Ahmadov, K.; Meyer, P.; Hachulla, A.-L.; Craviari, C.; Fontana, P.; Bendjelid, K.; Giraud, R. An Unusual Thrombus Location in a Heartmate 3TM Device with Fatal Outcome. *Perfusion* **2019**, 0267659119890218.
23. Ootaki, Y.; Kamohara, K.; Akiyama, M.; Zahr, F.; Kopcak Jr, M.W.; Dessoffy, R.; Fukamachi, K. Phasic Coronary Blood Flow Pattern during a Continuous Flow Left Ventricular Assist Support. *European journal of cardio-thoracic surgery* **2005**, *28*, 711–716.
24. Islam, S.; Cevik, C.; Madonna, R.; Frandah, W.; Islam, E.; Islam, S.; Nugent, K. Left Ventricular Assist Devices and Gastrointestinal Bleeding: A Narrative Review of Case Reports and Case Series. *Clinical cardiology* **2013**, *36*, 190–200.
25. Stern, D.R.; Kazam, J.; Edwards, P.; Maybaum, S.; Bello, R.A.; D'Alessandro, D.A.; Goldstein, D.J. Increased Incidence of Gastrointestinal Bleeding Following Implantation of the HeartMate II LVAD. *Journal of cardiac surgery* **2010**, *25*, 352–356.
26. Crow, S.; John, R.; Boyle, A.; Shumway, S.; Liao, K.; Colvin-Adams, M.; Toninato, C.; Missov, E.; Pritzker, M.; Martin, C. Gastrointestinal Bleeding Rates in Recipients of Nonpulsatile and Pulsatile Left Ventricular Assist Devices. *The Journal of thoracic and cardiovascular surgery* **2009**, *137*, 208–215.
27. Schlöglhofer, T.; Robson, D.; Bancroft, J.; Sørensen, G.; Kaufmann, F.; Sweet, L.; Wrightson, N. International Coordinator Survey Results on the Outpatient Management of Patients with the HeartWare® Ventricular Assist System. *The International journal of artificial organs* **2016**, *39*, 553–557.
28. Fraser, K.H.; Zhang, T.; Taskin, M.E.; Griffith, B.P.; Wu, Z.J. A Quantitative Comparison of Mechanical Blood Damage Parameters in Rotary Ventricular Assist Devices: Shear

Stress, Exposure Time and Hemolysis Index. *Journal of biomechanical engineering* **2012**, *134*.

29. Thamsen, B.; Blümel, B.; Schaller, J.; Paschereit, C.O.; Affeld, K.; Goubergrits, L.; Kertzscher, U. Numerical Analysis of Blood Damage Potential of the HeartMate II and HeartWare HVAD Rotary Blood Pumps. *Artificial organs* **2015**, *39*, 651–659.
30. Tsai, H.-M.; Sussman, I.I.; Nagel, R.L. Shear Stress Enhances the Proteolysis of von Willebrand Factor in Normal Plasma. **1994**.
31. Klovaite, J.; Gustafsson, F.; Mortensen, S.A.; Sander, K.; Nielsen, L.B. Severely Impaired von Willebrand Factor-Dependent Platelet Aggregation in Patients with a Continuous-Flow Left Ventricular Assist Device (HeartMate II). *Journal of the American College of Cardiology* **2009**, *53*, 2162–2167.
32. Letsou, G.V.; Shah, N.; Gregoric, I.D.; Myers, T.J.; Delgado, R.; Frazier, O.H. Gastrointestinal Bleeding from Arteriovenous Malformations in Patients Supported by the Jarvik 2000 Axial-Flow Left Ventricular Assist Device. *The Journal of heart and lung transplantation* **2005**, *24*, 105–109.
33. Casa, L.D.; Deaton, D.H.; Ku, D.N. Role of High Shear Rate in Thrombosis. *Journal of vascular surgery* **2015**, *61*, 1068–1080.
34. Bark, D.L.; Vahabi, H.; Bui, H.; Movafaghi, S.; Moore, B.; Kota, A.K.; Popat, K.; Dasi, L.P. Hemodynamic Performance and Thrombogenic Properties of a Superhydrophobic Bileaflet Mechanical Heart Valve. *Annals of biomedical engineering* **2017**, *45*, 452–463.
35. Colace, T.V.; Diamond, S.L. Direct Observation of von Willebrand Factor Elongation and Fiber Formation on Collagen during Acute Whole Blood Exposure to Pathological Flow. *Arteriosclerosis, thrombosis, and vascular biology* **2013**, *33*, 105–113.
36. Nesbitt, W.S.; Westein, E.; Tovar-Lopez, F.J.; Tolouei, E.; Mitchell, A.; Fu, J.; Carberry, J.; Fouras, A.; Jackson, S.P. A Shear Gradient–Dependent Platelet Aggregation Mechanism Drives Thrombus Formation. *Nature medicine* **2009**, *15*, 665–673.
37. Zheng, X.L. ADAMTS13 and von Willebrand Factor in Thrombotic Thrombocytopenic Purpura. *Annual review of medicine* **2015**, *66*, 211–225.
38. Cowger, J.A.; Romano, M.A.; Shah, P.; Shah, N.; Mehta, V.; Haft, J.W.; Aaronson, K.D.; Pagani, F.D. Hemolysis: A Harbinger of Adverse Outcome after Left Ventricular Assist Device Implant. *The Journal of heart and lung transplantation* **2014**, *33*, 35–43.
39. Morshed, K.N.; Jr, D.B.; Forleo, M.; Dasi, L.P. Theory to Predict Shear Stress on Cells in Turbulent Blood Flow. *PLOS ONE* **2014**, *9*, e105357, doi:10.1371/journal.pone.0105357.
40. Loor, G.; Gonzalez-Stawinski, G. Pulsatile vs. Continuous Flow in Ventricular Assist Device Therapy. *Best Practice & Research Clinical Anaesthesiology* **2012**, *26*, 105–115.
41. Starling, R.C.; Moazami, N.; Silvestry, S.C.; Ewald, G.; Rogers, J.G.; Milano, C.A.; Rame, J.E.; Acker, M.A.; Blackstone, E.H.; Ehrlinger, J. Unexpected Abrupt Increase in Left Ventricular Assist Device Thrombosis. *New England Journal of Medicine* **2014**, *370*, 33–40.
42. Roche, E.T.; Horvath, M.A.; Wamala, I.; Alazmani, A.; Song, S.-E.; Whyte, W.; Machaidze, Z.; Payne, C.J.; Weaver, J.C.; Fishbein, G. Soft Robotic Sleeve Supports Heart Function. *Science translational medicine* **2017**, *9*.
43. Schulz, A.; Krabatsch, T.; Schmitto, J.D.; Hetzer, R.; Seidel, M.; Dohmen, P.M.; Hotz, H. Preliminary Results from the C-Pulse® OPTIONS HF European Multicenter Post-Market Study. *Medical science monitor basic research* **2016**, *22*, 14.

44. Chair, S.Y.; Yu, D.S.; Ng, M.T.; Wang, Q.; Cheng, H.Y.; Wong, E.M.; Sit, J.W. Evolvement of Left Ventricular Assist Device: The Implications on Heart Failure Management. *Journal of geriatric cardiology: JGC* **2016**, *13*, 425.
45. Snyder, T.; Bourquin, A.; Cornat, F.; Biasetti, J.; Botterbusch, C. Corwave LVAD Development Update. *The Journal of Heart and Lung Transplantation* **2019**, *38*, S341–S342.

CHAPTER 2: EMBRYONIC HEART PUMPING MECHANISM

2.1 INTRODUCTION

The heart is the first developing organ and functions before its own morphology is completely developed [1]. Structurally, it is tubular in shape when it begins pumping blood through the body without the benefit of valves. The heart tube consists of an inner endocardium, a middle layer of extracellular matrix (cardiac jelly) and an outer cardiomyocyte monolayer (myocardium). Different sections of the heart are activating during the cardiac cycle, unidirectional from the inlet to the outlet. Active contractile patterns of the myocardium, combined with mechanical properties, dictate the pumping behavior that drives blood flow.

Peristalsis and impedance pumping have both been introduced as potential pumping behaviors at the early stages of embryonic heart development, and neither mechanism necessitates a valve [2–9]. Peristalsis involves an actuating region that travels as a wave, thereby displacing a volume of fluid. Impedance pumping relies on pressure waves generated by periodic compression of an elastic tube at a single location in space. Pressure waves propagate along the tube's walls, reflecting at the tube's extremities with superposition that overall drives the flow in one major direction. An advantage of the latter is that contraction is only required a single location along the tube. However, impedance pumping is highly reliant on surrounding mechanical properties [2,5,6].

Numerical methods have been useful for investigating pumping behavior, since they enable the interrogation of parameters, like mechanical properties. Methods to study pumping come in two forms: one-way and two-way structural coupling. In one-way coupling, wall motion is fully controlled, impacting upon the surrounding fluid [9–13]. Studies that use this approach find that peristaltic pumping is capable of delivering a physiological cardiac output (CO) [9–13].

Two-way coupled Fluid-Structure Interactions (FSI), enable fluid forces to affect the surrounding solid domain [2,14,15] - such an approach is required to study impendence pumps, while remaining amenable to peristaltic pumping. Studies using two-way FSI method with a 1 Pa cardiac wall suggest that peristaltic pumping provides an insufficient CO and pressure (Kozlovsky et al. 2016). More recently, studies indicate that the heart tube may exhibit both peristaltic and impedance pumping behavior, with volume displacement-like pumping that is enhanced by pressure wave superposition, termed "biological pumping" [7]. The precise influence of mechanical properties on these models remains unclear.

Several computational studies [2,7,16–18] assume that the stiffness of the myocardium is on the order of 1 Pa. We recently discovered that mechanical behavior is better described by a Neo-Hookean model with a material constant on the order of 10 kPa, for zebrafish [19]. Furthermore, cultured cardiomyocytes function optimally, that is to say, by maximum force production, in an environment with the material constant of of 10 kPa [20–24]. Therefore, either cardiomyocytes work in a range that does not optimize their force production [22–25] or, the embryonic myocardium may be stiffer than previously considered in computational work, spurring the question of what influence the mechanical properties could have on pumping.

To determine the impact of stiffness on pumping function, we developed a FSI computational model of the embryonic zebrafish heart. An FSI technique enables two-way coupling between mechanical properties and pumping behavior. Behavior is compared with experimental measurements of blood flow through a zebrafish at 30 hours post-fertilization (hpf). We chose these two values for the material constants based on the reported values in the prior studies and the most recent findings. Moreover, we have not seen a two-way FSI study which considers the material constant in the range of 10 kPa.

2.2 METHOD

All experiments on embryonic zebrafish were approved by the IACUC at Colorado State University. Embryos were collected immediately after fertilization and incubated for 30 hours at 28˚C. Embryos were confirmed to be in the mid- to late-heart tube stage, which takes place between 24 and 30 hpf [26]. Selected embryos were dechorionated and placed in a solution of E3 embryo medium for holding. Individual embryos were moved to a coverslip and embedded in 1.5% low-melt agarose to arrest movement for imaging, performed on an inverted microscope (Olympus IX73 with 20X objective and the optical resolution of 0.37- 0.45 microns) using a high-speed camera (Photron Fastcam Mini UX100) at 1600 frames per second. 3-4 cardiac cycles were recorded, and heart function was analyzed using a spatiotemporal plot analysis, similar to what we have done previously [27]. Briefly, a reference line was created at the atrial inlet in the direction of flow (Fig. 2.1a) to calculate the speed of passing red blood cells (RBC)s. An ensemble average of velocity was taken over all cardiac cycles (3-4) for a given fish. In addition to calculating blood velocity, we quantified the relative coordinates of the endocardium by manually tracing the cells using ImageJ, where a representative zebrafish was used for comparison with simulation results [15].

A computational simulation was developed to model the zebrafish heart at 26-30 hpf based on idealized cylindrical geometry (Fig. 2.1b). A cylindrical tube provides us with the ability to use an axisymmetric simulation, which greatly reduces the otherwise expensive computational cost of an FSI simulation. This enables us to efficiently and systematically assess the variables studied in the current work. Our model consists of a two-layer wall, with 1 layer to simulate the myocardium and 1 to simulate the cardiac jelly and endocardium based on morphological data (shown in Fig 2.1b, c) [3,28][29,30]. The heart tube is assumed axisymmetric [9,17]. We used 3 core processor and the computational time for each processor is 15 to 30 minutes based on the pumping mechanism. The lumen diameter is defined as 50 µm, extending to a length of 180 µm, with a 12 µm thick cardiac jelly and a 3.5 µm thick myocardium, thereby matching experimental dimensions. Mechanical properties are assumed homogeneous along the entire length of the tube.

Arbitrary Lagrange Eulerian formulation in COMSOL Multiphysics (COMSOL Inc., Burlington, MA) is used to simulate fluid flow and boundary deformation. The solid extremes are fixed to have an impedance mismatch [2], an important feature for impedance pumping. A viscosity model has not been experimentally verified during early zebrafish development, but since blood at the heart tube stage involves only a dilute suspension of nucleated erythrocytes, we assumed it be Newtonian. A Lagrangian–Eulerian method with Winslow smoothing is used to solve the moving boundary in the fluid domain. We assume that solid domains can be described by a Neo-Hookean constitutive equation. Grid-independence was confirmed, with an optimum number of grid points of 15,000 for the solid domain and 55,000 for the liquid domain. No-slip boundary conditions are applied at the fluid–structure interface. Pressure at the fluid domain inlet is set to zero, simulating the venous return. The pressure at the outlet is defined from a 0D model of embryonic circulation [31] shown in Fig. 2.1c,

$$\mathrm{C}\frac{\mathrm{dP_{out}}}{\mathrm{dt}} = \mathrm{Q_{out}(t)} - \frac{\mathrm{P_{out}}}{\mathrm{R}} \qquad (1)$$

$Q(t)$ is the flowrate at the outlet of the heart tube, which depends on the specific simulation. C is compliance and R is the vascular resistance. The same values of the vascular resistance and compliance are used for all pumping functions since the vasculature should be independent of the function.

Two material constants are used to model the myocardial behavior in the study: 60 Pa based previous studies [7,16,18] and 10 kPa, where cultured cardiomyocytes produce a maximum force [20–24]. It is assumed that the material constant of cardiac jelly is 10% of the myocardium [7,17,18]. The parameter values for each case and the range of the variables are shown in Table 2.1. We chose extremely low stiffness values because the majority of prior literature [7,16,18] uses this value to investigate pumping mechanics of the embryonic heart tube. We want to compare what impact our new-found 'stiffness' would have on the fluid mechanics. The tubular heart pumping mechanism is possibly misjudged in several studies which considered the heart as a very elastic material. However, combined with the modulus typical of cells and what we've recently found; the material constant needs to be in the range of 10 kPa. To have a comparative study between the reported value and our founding, we used the mentioned two values.

Table 2.1. Parameters for numerical simulations

Parameter	Unit	Value	Reference
Myocardium thickness	μm	3.5	experiment
Cardiac jelly thickness	μm	12	experiment
Heart length	μm	180	experiment
Lumen diameter	μm	50	experiment
Blood density	kg/m^3	1035	[11,14]
Blood viscosity	Pa.s	0.008	[12,33]
Heart rate	bpm	120	experiment
Wavelength of contractions	μm	60-90	experiment
Vascular resistance	mmHg.s/mm^3	60	[9,27]
Compliance	mm^3/mmHg	0.26	assumption
Poisson's ratio	-	0.49	assumption
Myocardium material constant	Pa	60 &10,000	[7,16,18]& [19–24]
Cardiac jelly material constant	Pa	4	[29,30]

When cardiomyocytes contract, they effectively generate an axial and circumferential force along the heart tube, while passive restorative forces exist from surrounding mechanical properties. The applied force to compress the heart tube is defined as either a: peristaltic, impedance, or muscle function based on the following load distributions [7,9]. For peristaltic pumping, we use:

$$\mathrm{F}_p(\mathrm{z},\mathrm{t}) = \sin^2\left(\frac{\pi\,\mathrm{z}}{\lambda} - \pi\,\mathrm{HR}\,\mathrm{t}\right), \tag{2}$$

where λ is the wavelength of contraction and *HR* is the heart rate [7], Fig. 2. 2a. z is the axis along the heart tube and *t* is time. The impedance pumping function used in this study is:

$$\mathrm{F}_i(\mathrm{t}) = \sin^2\left(\frac{\pi\,\mathrm{HR}\,\mathrm{t}}{\tau}\right) \qquad \mathrm{t}_1 < \mathrm{t} < \mathrm{t}_2 \qquad \Delta\mathrm{t} = (\mathrm{t}_2 - \mathrm{t}_1) \qquad \tau = \Delta\mathrm{t}/(\mathrm{T} - \Delta\mathrm{t}), \tag{3}$$

where $t_1$is the time that contraction engages (time 0) and $t_2$is the time that contraction disengages (time 0.2T) based on experiments, Fig. 2.2b. *T* is the duration of the cardiac cycle (1/HR). This function applies along the active length of the tube near the inlet (0.2L), Fig.2.2b. The muscle function for this study is defined as:

$$\mathrm{F}_{mf}(\mathrm{z},\mathrm{t}) = (\mathrm{H}(\mathrm{t}-\mathrm{t}_1) - \mathrm{H}(\mathrm{t}-\mathrm{t}_2)) \times \exp\left[-0.5 \times \left(\frac{\mathrm{z}}{\mathrm{L}} - \mathrm{HR}\,\mathrm{t}\right)^2\right] \qquad \mathrm{t}_1 < \mathrm{t} < \mathrm{t}_2, \tag{4}$$

where H(t) is the Heaviside function, Fig. 2.2c. *L* is the length of the heart tube. The zebrafish cardiac muscle function is based on the calcium flux in the mice embryonic heart at the same stage [25,32–34], that was previously developed for skeletal muscle [33].

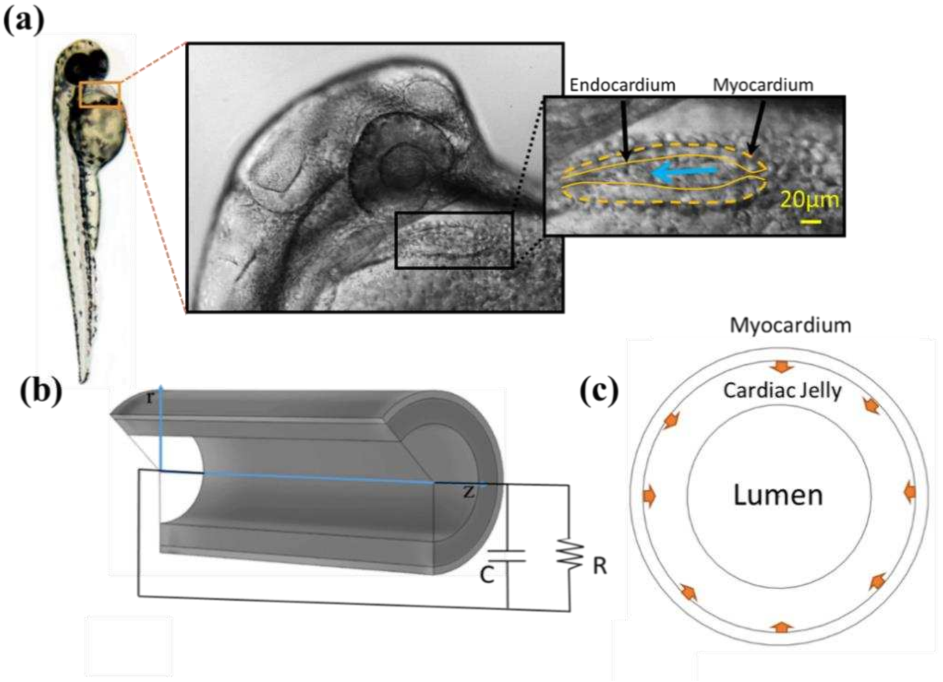

Figure 2.1. (a) Image of a 30 hpf embryonic zebrafish head and heart (enlarged inset on right). The myocardium is indicated by the dashed line. The endocardium represents the flow boundary and is indicated by the solid line. The cardiac jelly exists between these two layers. The blue arrow indicates flow direction. (b) Axisymmetric model representation of the heart tube. R is vascular resistance and C is the compliance (c) Layers of the heart tube model in a cross-sectional view, where the endocardium is assumed to be of the same mechanical properties as the cardiac jelly. Arrows show the contraction of the myocardium.

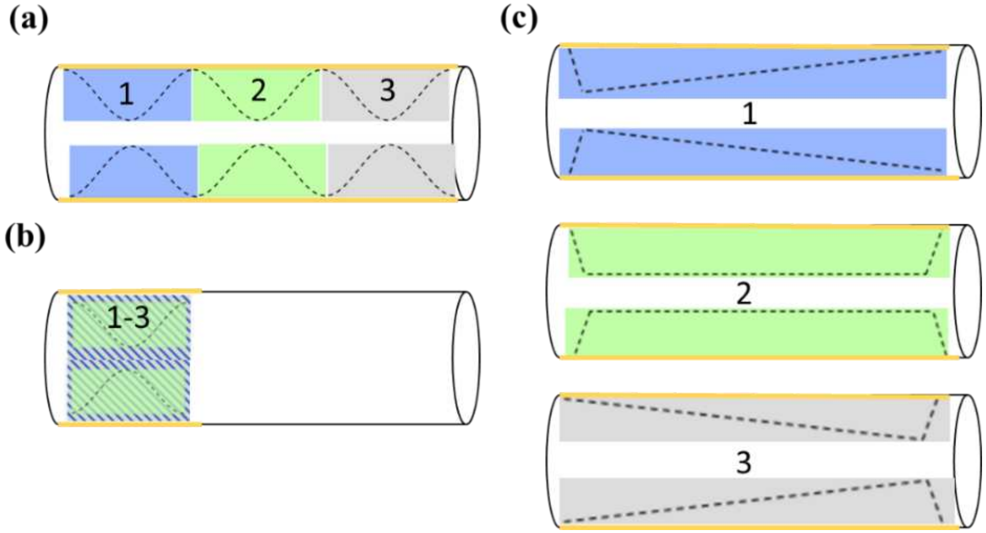

Figure 2.2. Contraction motion for each pumping function (a) peristaltic, (b) impedance, and (c) muscle function. Numbers 1-3 shows the contraction motion in time along the heart with 1 being the start of contraction and 3 being the end of contraction. The active region in each pumping function is shown with yellow color on the wall.

We calculate the energy out of the heart by using the following equation:

$$\mathrm{E_{out}} = \int_0^T \mathrm{P}_{out}\,(\mathrm{t}) Q_{out}(t) dt$$

(5)

Where P is the blood pressure and $Q_{out}(t)$ is the cardiac output.

We approximate the work done in the following calculations with assuming an incompressible thin-walled cylinder:

$$ltr = LTR \rightarrow lt = \frac{LT}{\lambda}$$

$$W_d = 2\pi(lt\sigma_c)(R - r) = 2\pi\sigma_c\left(\frac{LTR}{\lambda} - ltr\right) = 2\pi\sigma_c LTR\left(\frac{1}{\lambda} - 1\right) = 2\pi\sigma_c V\left(\frac{1}{\lambda} - 1\right) \tag{6}$$

Where *T, L* and *R* are the initial thickness, length and radius which updates in each timestep, and σ_c is the circumferential stress in the active area. The cardiomyocyte length is assumed 20 µm [22,35].

Note that the total work done is the summation of work done from all cardiomyocytes, as opposed to the work done by a single cardiomyocyte, Eq. 6. We calculated the efficiency by dividing the values of energy out to total work done for different pumping functions and material constants.

$$\text{Efficiency} = \frac{\mathrm{E_{out}}}{\mathrm{W_d}} \times 100 \tag{7}$$

2.3 RESULTS

Based on the experimental results for the zebrafish embryonic heart at 30 hpf, the heart rate (HR) and cardiac output (CO) are 120 beats per minute (bpm) and 0.02 µL/min respectively, with deformation shown in Fig 2. 3a. Experimental Reynolds and Womersley numbers are respectively 0.11 and 0.02, demonstrating that viscous forces dominate over inertia and transient forces. Fig. 2. 3b-d shows the simulated peristaltic, impedance, and muscle functions' wall deformation throughout one cardiac cycle (Eqn. 2-4) for the material constant of 60 Pa and 10 kPa. Peristaltic pumping (Eqn. 2) leads to a traveling wave that starts at the inlet and continues to the outlet, where it dissipates as the next wave of contraction initiates at the inlet, regardless of the stiffness (Fig.2. 3b, 4e). In impedance pumping (Eqn. 3), there is an active zone near the inlet, while the rest of the heart is passive, leading to local compression of the lumen due to contraction in the active zone (Fig. 2.3c and f). This causes downstream passive inflation due to pressure waves that generate circumferential stress (theoretically proportional to the local axially varying pressure). The pressure wave travels through the tube for 0.8T. For the 10 kPa heart, the pressure wave lasts for less than 0.4T. For the muscle function (Eqn. 4), contraction starts near the inlet, travels to the middle of the heart, and continues occluding near the outlet as a wave of relaxation begins at the inlet (Fig. 2. 3d and g), overall leading to a longer region of constriction that can create more resistance to backflow. In summary, the material constants, and pumping functions (Eq. 2-4) strongly influence the wall deformation patterns.

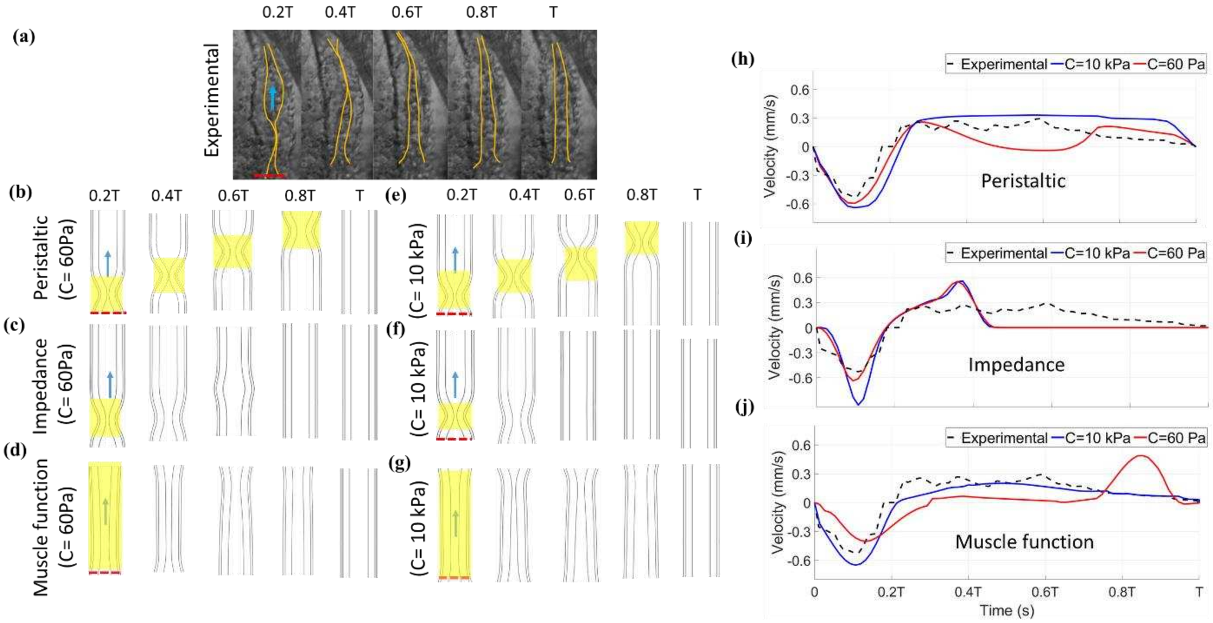

Figure 2.3. Heart wall motion (myocardium and cardiac jelly) during one cardiac cycle for an (a) experiment, as well as for the stiff model (E=10 kPa) using (b) peristaltic, (c) impedance, and (d) muscle functions with a comparison to a model of lower material constant (60 Pa) using (e) peristaltic, (f) impedance, and (g) muscle functions. Flow direction is shown by an arrow and the dashed red line depicts the inlet to the heart, where contractions begin. The active region in each pumping function is shown with yellow highlight for each pumping function. Axial velocity is also compared between the experimental results at the inlet (dashed red line) relative to simulation results for (h) peristaltic, (i) impedance, and (j) muscle functions.

To quantitatively relate wall deformation patterns to hemodynamics, representative experivamental velocity measurements at the atrial inlet are compared with the numerical results for a myocardial material constant of 60 Pa and 10 kPa (Fig. 2.3h-j). The inlet is chosen because the outlet is obscured in experiments involving zebrafish. Experimentally, there is retrograde flow at the inlet as contraction initiates in experiments since blood is initially pushed bidirectionally as the lumen begins to constrict, in a region slightly shifted from the inlet (~3µm). The retrograde flow at the inlet is seen in every simulated pumping mechanism as well. After initial reverse flow, a compressive wave travels along the channel, as fluid is forced to the outlet. Blood at the inlet begins to move forward once the myocardium begins to relax near the inlet. The relaxation wave occurs at a rate of approximately 0.25 mm/s, roughly matching the velocity of blood cells at the center of the heart. Blood cells move in the forward direction throughout relaxation until contraction begins again at the inlet. Overall, despite initial reverse flow that dissipates quickly in the relatively large sinus venosus, the heart tube is capable of driving blood forward.

Hemodynamics from simulated pumping can provide insight into mechanical properties and active pumping functions. Peristaltic pumping for the 60 Pa wall exhibits reverse flow with a similar magnitude as the experiment, whereas the much stiffer 10 kPa heart produces a 1.5 times larger reverse velocity (Fig. 2.3h). The difference is characteristic of a "Windkessel" model as discussed by [36] $\mathrm{Q(L,t) = Q(0,t) - C\frac{dP}{dt}}$, where Q is the flow rate, l is the distance from the point of contraction to the inlet, C is compliance, t is time, and P is pressure [36]. Therefore, for an inlet with a relatively constant area, the velocity will increase as compliance decreases (elastance increases), for a given flow rate in the contractile region, Q(0,t). Essentially, a compliant vessel will absorb some fluid volume during contraction. Correspondingly, the wall expands out further due to the compliance, as seen in Table 2.2. As time continues, forward flow occurs, reaching a peak velocity of 0.3 mm/s. The heart with the material constant of 60 Pa shows a sudden drop in axial velocity, while the 10 kPa heart continues to drive flow forward with a similar peak velocity as the experiment. The velocity difference can again be attributed to a compliance difference characterized through a "Windkessel" model, where the radius of the tube expands 3 μm for the more compliant heart in Table 2.2. Note that the velocity is relatively constant in the 10 kPa simulation since peristalsis in a stiff heart should lead to velocity that is proportional to the constant contraction/expansion wave speed. In the experiment, velocity follows a similar trend, but exhibits a slow decrease earlier during diastolic filling. The impedance pumping function exhibits reverse flow and then an overshoot in axial velocity before quickly dropping to a value of

0 (Fig. 2.3i) for both stiffness values. It lacks a sustained flow output. When the material constant is 60 Pa, the maximum velocity is 1.5-fold smaller than the stiffer heart as the wall expands in response to pressure, Table 2.2. It's acknowledged that the impedance pump requires specific pumping frequencies and specific compliance mismatches at boundaries for optimum pumping, with the former being further evaluated in the next section. Fig. 2.3j shows the muscle function, which exhibits backflow due to the contraction near the inlet and a slightly over-damped response during forward flow for the heart with material constant of 10 kPa. Very little flow is seen for the 60 Pa heart, except near the start and end of contraction. In the elastic heart with the muscle function contraction pattern, the lumen stays open due to fluid pressure and the outlet pressure and flow stays low. Wall material properties appears to play a lesser role in the muscle function since radial expansion in table 2. 2 is relatively unaffected and since the majority of the heart experiences diffuse active contraction, as opposed to the small segment of active contraction in the other functions. Diffuse active contraction is the contraction expansion along the heart tube. Quantitatively, there is 26%, 29% and 13% variance ($\text{Variance\%} = 100\% \cdot \sum \frac{|Value_{PM} - Value_{EX}|}{Value_{EX}}$) respectively for the peristaltic, impedance, and muscle functions relative to the experiment for the material constant of 10 kPa, where $Value_{PM}$ is the simulated velocity and the $Value_{EX}$ is the experimental velocity. These values for the more compliant 60 Pa heart are 30%, 29% and 39%. Overall, the 10 kPa muscle function axial velocity matches best with experimental results.

Table 2.2. The radial expansion during a cardiac cycle for different pumping functions

Pumping function	Material constant (Pa)	Maximum radial expansion (μm) 0-3 μm from inlet	Radial expansion (μm) 3-180 μm from inlet
Peristaltic	60	0.7	1.3
	10k	0	0.1

Impedance	60	0	0.9
	10k	0	0.3
Muscle function	60	0	0.1
	10k	0	0

Blood pressure produced by the heart is important for driving flow throughout the circulation. Fig. 2. 5 shows the systolic blood pressure for all pumping functions at a HR of 120 bpm at the outlet. The green dashed line is the expected systolic pressure based on values reported in the literature [37–39]. The stiffer myocardium with the material constant of 10 kPa provides a sufficient systolic pressure (Fig. 2.4a, c) for peristaltic and muscle functions. Pressure is also sustained at the outlet in these two cases, which can lead to longer period of forward systolic flow due to a pressure differential existing across the heart for a longer period of time (note that pressure at the inlet is set to 0). Impedance pumping cannot provide a systolic pressure that matches previously reported values and only produces a high pressure for a very short duration <0.2T (Fig. 2.4b). In the impedance pumping mechanism, the heart stiffness is damping the waves. The stiffer heart damps the waves faster than the elastic heart. Overall, a stiff heart with sustained active contraction is necessary, seen in peristaltic and muscle function, to produce a sustained high pressure at the outlet for the current models.

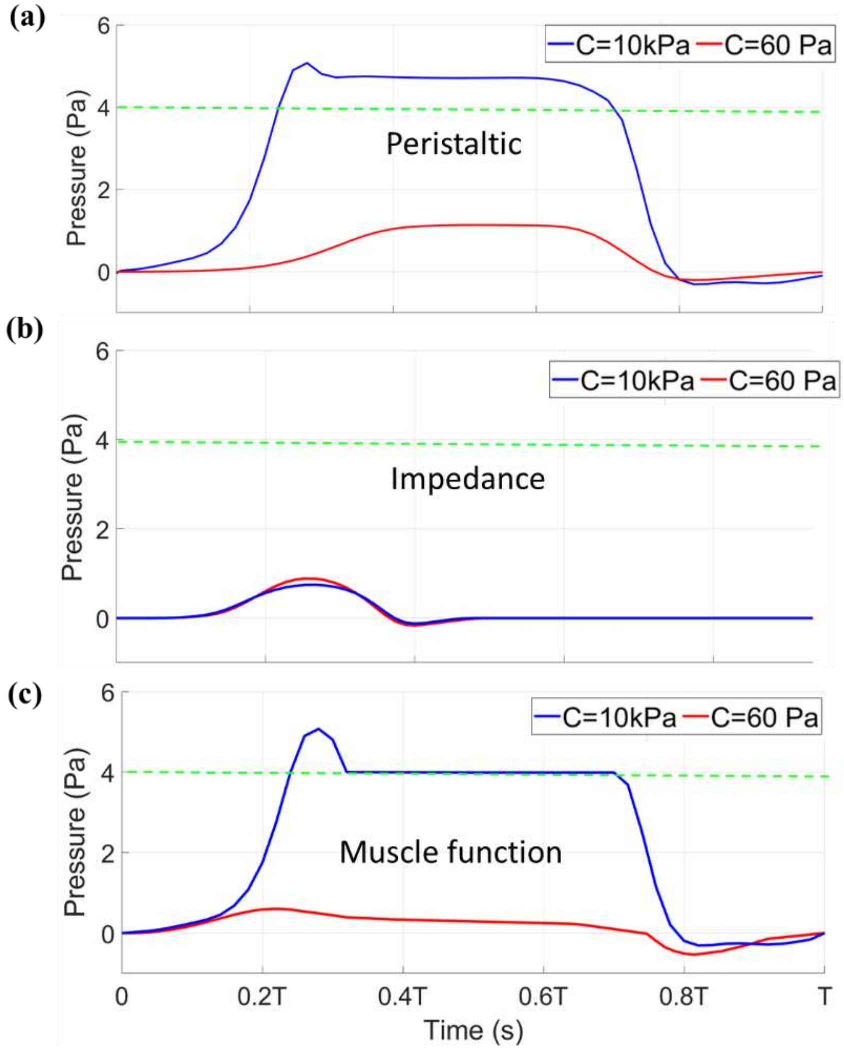

Figure 2. 4. Systolic pressure comparison between the material constant of 60 Pa (red line) and 10 kPa (blue line) in (a) peristaltic, (b) impedance, and (c) muscle function pumping functions with respect to time normalized by the period of a complete cardiac cycle. The green dashed line shows the reported systolic pressure from the literature (4 Pa).

The circumferential stress on the solid wall and the fluid pressure plotted on an axial slice are shown in Fig. 2.5a-c. Contractile mechanics are largely dictated by the active and passive circumferential stress in the wall. As seen in Fig. 2.5a-c, circumferential stress is highest in regions of active contraction and in the case of impedance pumping, it remains high along the traveling pressure wave. This leads to concentrated regions of circumferential stress in peristaltic and impedance pumping compared to more diffuse circumferential stress seen in the muscle function that actively contracts over a larger region. In addition to differences related to the pumping function, stress is higher for a stiffer wall in the simulations since active contraction is created by defining a radial contractile force in each pumping function, such that the force nearly collapses the lumen without creating contact (due to limitations in FSI simulations). Since less force is required for this purpose in the 60 Pa heart, there is less circumferential stress. Overall, an active force creates a region of high circumferential stress to deform the heart tube, thereby increasing pressure that drives fluid forward, while circumferential stress patterns change depending on the pumping function and stiffness.

The axial and circumferential wall stress is integrated through Eq. 6 to determine the approximate work done during one cardiac cycle to support peristaltic, impedance, and muscle function pumping, which is shown in Fig. 2.5(d). It is noted that work is only performed while the cardiomyocyte is actively contracting (a fraction of the overall cardiac cycle) and the effect of the axial wall stress is almost negligible. The amount of work done is higher for a stiffness of 10 kPa when compared with 60 Pa for all pumping functions due to the higher specified contractile force. Peristaltic and impedance pumping results in a shorter interval of contraction per cardiomyocyte, thereby leading to less work done per cell, when compared to the diffuse long phase of contraction per cardiomyocyte specified for the muscle function. Altogether, work done by a cardiomyocyte is lowest for the impedance function and highest for the muscle function.

Global cardiac energetics are also quantified. Fig. 2.5e shows the energy exiting the heart in each cardiac cycle. The peristaltic and muscle function pumping functions produce the most energy for the material constant of 10 kPa, leading to comparable energy seen in experiments [37]. This is due to ability of these pumping functions to provide the highest CO and pressure. The energy out from impedance pumping is much lower for both stiffness values. Energy efficiency for peristaltic, impedance, and muscle functions when the material constant of myocardium is 10 kPa is 1.7%, 0.1%, and 0.57% respectively, while the corresponding values for the more compliant myocardium (60 Pa) are 18.5%, 1.2% and 10.3% respectively (Fig. 2.5f). Based on these results, the stiffer heart is less efficient, as cardiomyocytes overcome the wall stiffness to generate a contractile wave, yet a stiffer heart is required to obtain a physiologic energy output.

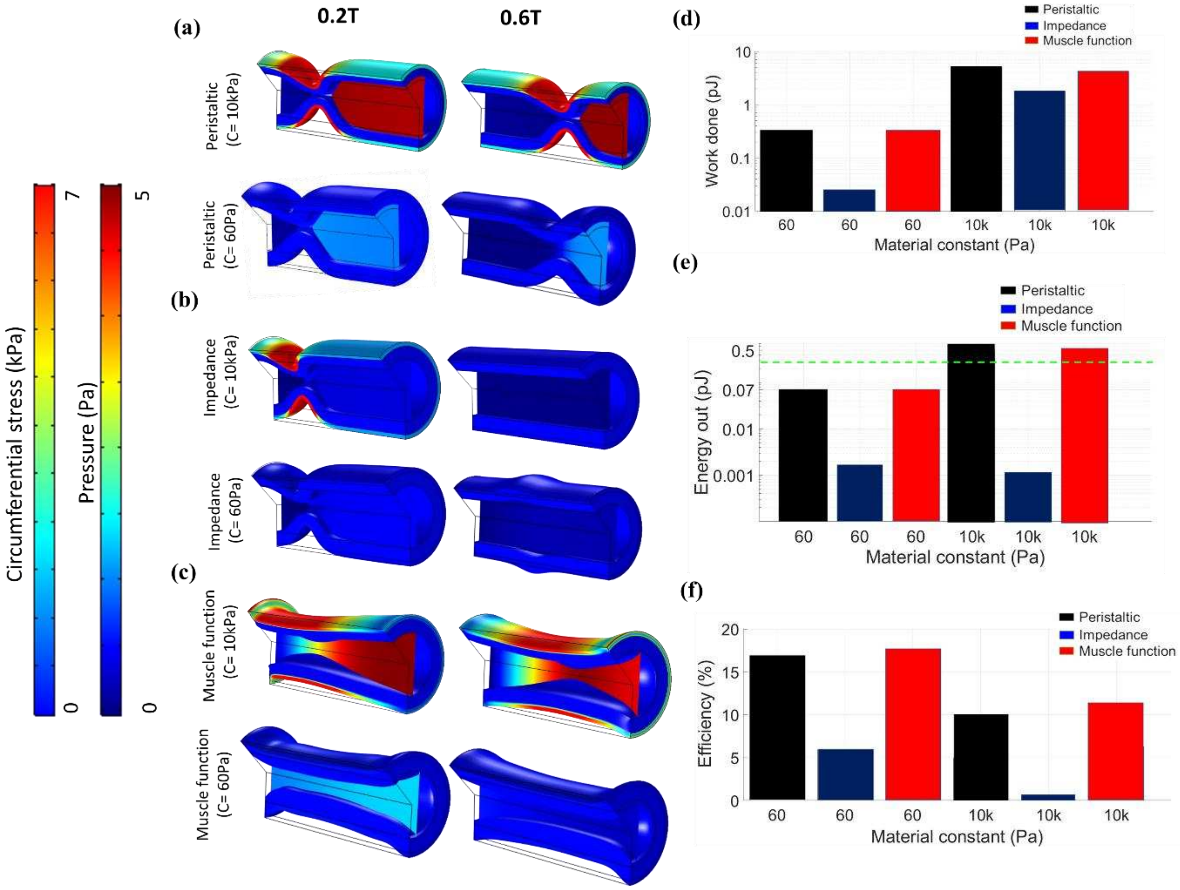

Figure 2.5. Solid circumferential stress and fluid pressure contours plotted on an axial slice at two time points during the cardiac cycle for 60 Pa and 10 kPa pertaining to (a) peristaltic, (b) impedance, and (c) muscle functions. (d) Work done (log scale) by each cardiomyocyte for each pumping function for the material constant of 60 Pa and 10 kPa. (e) Energy out (log scale) from the heart for each pumping function for material constant of 60 Pa and 10 kPa. The experimental value of the energy out from the zebrafish heart at this stage is shown by the green dashed line comes from the literature. (f) efficiency of each pumping function for material constants of 60 Pa and 10 kPa.

The HR (or pumping frequency) can impact upon the pump's output based on both pumping functions and mechanical properties. A healthy zebrafish HR during early development ranges from 80-120 bpm at room temperature. Fig. 2.6a demonstrates that a peristaltic function with a stiff myocardium (10 kPa) can provide a CO that matches experiments, while a 60 Pa myocardium underestimates CO for HRs within this range. CO for the HRs below 60 bpm and above 240 bpm are not shown since these HRs would be abnormal for embryonic zebrafish. Note that the CO increases with HR since a peristaltic pump functions as a volume displacement pump, where faster contractile wave translation leads to faster rates of volume displacement. Impedance pumping does not provide a sufficient CO (Fig. 2.6b) regardless of stiffness for any HR based on operating conditions. Hearts with the muscle function provide the optimal CO for a HR of 120 bpm, which is a typical HR for zebrafish at the studied stage of development. The experimental CO value is just used as a benchmark to examine different pumping mechanism. HR was not varied in our experiments; it was only varied in the simulations otherwise the CO for each HR is a different value. Overall, these results demonstrate that the optimal CO can be provided when the myocardial material constant is on the order of 10 kPa, except for the impedance pump case, which cannot provide the optimal CO regardless of material constant for the current simulation.

Overall, an FSI simulation of the embryonic heart tube demonstrates that hemodynamics match between embryonic zebrafish at 30 hours postfertilization when the myocardial stiffness is on the order of 10 kPa. However, while a stiff heart produces the greatest pressure and flow, it does so at a cost in efficiency when compared to a more compliant heart. This is because contraction must overcome the stiffness of the surrounding cells. 60 Pa is commonly assumed as the embryonic myocardial stiffness in computational studies. In present simulations, 60 Pa cannot produce a sufficient CO and pressure, without requiring a higher contractile force that would lead to compression of the cardiac jelly and endocardium – a potentially damaging scenario due to tribological interactions. Results show that the myocardium is likely stiffer in zebrafish than what has been previously modeled when evaluating pumping, which is in agreement with recent findings through measurements made during cardiac pressurization experiments, while peristaltic and muscle functions provide a sufficient hemodynamic output that matches experiments [19]. The prior studies might change if a stiffer value were used.

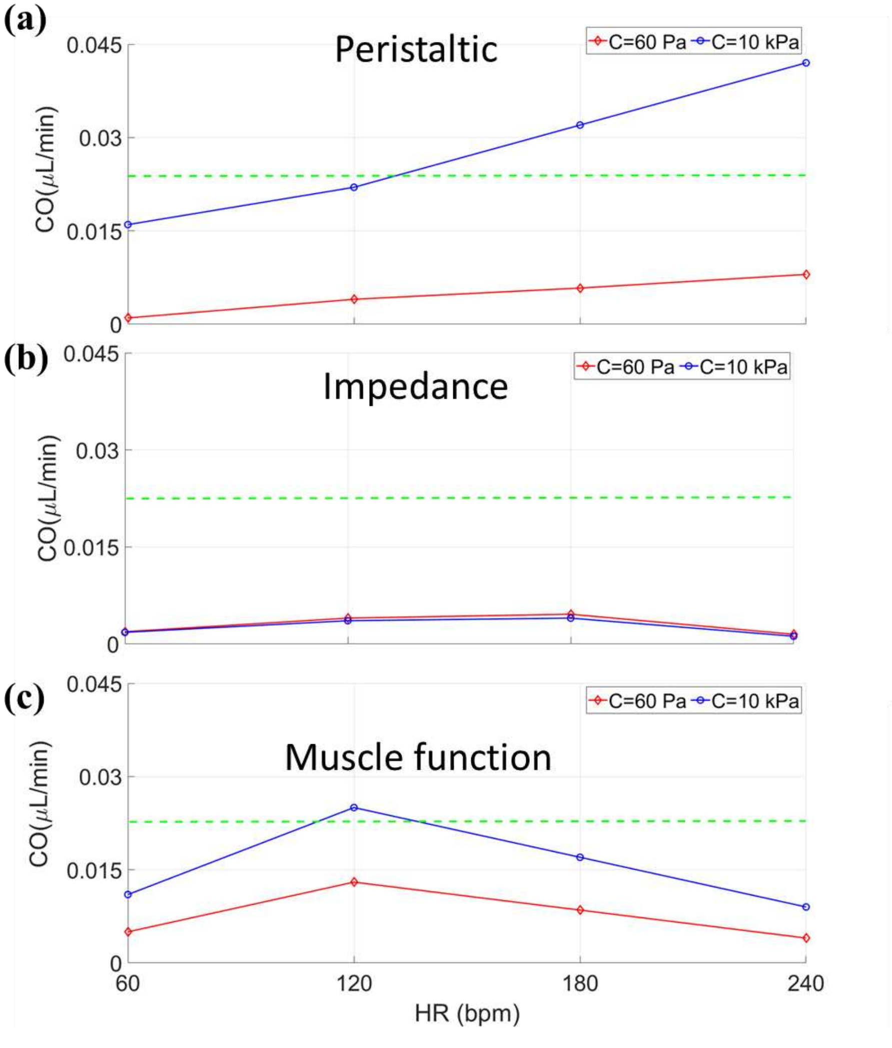

Figure 2.6. Cardiac output relative to heart rate (HR) for myocardial mechanical properties of 60 Pa (red line) and 10kPa (blue line) in (a) peristaltic, (b) impedance, and (c) muscle function pumping functions. The green line shows the cardiac output coming from the experiment (experimental value for CO is 0.02 μL/min).

It is critical to consider the actual output that a cardiomyocyte has for a given stiffness to assess whether the simulation accurately captures the cellular biophysics. Most experimental studies demonstrate that cardiomyocytes function poorly when cultured on a substrate stiffness below 1 kPa and they exhibit a rounded morphology without strong surface tethering [20–24,40,41]. On a 1 kPa substrate (compared to the 60 Pa compliant case), a cardiomyocyte can produce roughly 100 nN, with a resting force of 20 nN with ~167 Pa contractile stress. Alternatively, on 10 kPa, a cardiomyocyte can produce >700 nN of force, leading to ~ 940 Pa of contractile stress [23]. The latter is a value that is on the order of the circumferential stress values seen in current simulations. Furthermore, energy produced per cardiomyocyte in the simulation (for these contractile forces) for a 10 kPa heart is a fraction of what a cultured cardiomyocyte can produce (1.5 pJ) on a 10 kPa substrate, also indicating that a 10 kPa myocardium operates within the constraints of a cardiomyocyte's capability [21,22,24]. However, these arguments for a stiff substrate do not preclude cardiomyocytes from operating in a range where their force production is below optimal levels, like in the case of a 60 Pa heart. However, it is noted that lower force production would limit the pressure that can be produced by the heart, thereby limiting the driving force for blood flow. It is noted that the collective behavior of cardiomyocytes in a cylindrical sheet are not well-characterized. Therefore, the study does not fully confirm or negate the potential of a low material constant based on energy and stress requirements. However, for optimal force production and for an output expected from the heart, it may be necessary for the cardiomyocytes to be in an environment involving a large material constant (10 kPa). Note that stiffer hearts require more active stress for contraction compared to more compliant hearts and therefore there is likely a balance of stiffness with force production capability from cardiomyocytes to optimize efficiency.

In the current work, both peristaltic and muscle functions operate with the greatest output when the myocardium is 10 kPa, matching our recent measurements [19]. In agreement with others, peristalsis that occurs instead at 60 Pa provides an insufficient CO and systolic pressure, Fig. 2.4c and Fig. 2.6c [7]. The current work demonstrates that deformation of the 60 Pa myocardium is the primary cause for insufficient pumping. First, as pressure builds during pumping, the 60 Pa lumen expands, limiting the ability to resist backflow (Table 2.2, Fig. 2.5a and c). Furthermore, compliance of the heart wall leads to storage of blood volume and energy, limiting the pressure rise and peak velocity, Fig. 2.3h and j, and Fig. 2.4a and c. In terms of a 10 kPa heart, the primary difference in output between peristalsis and the muscle function is the heart rate dependence. The CO output is maximized at a HR of 120 BPM for the muscle function, whereas a peristaltic pump leads to increasing CO with HR. The former may provide benefit by limiting the CO to a maximum. Furthermore, this relation to heart rate has been previously reported in the literature through experiments [3]. Alternatively, an increasing CO with HR could hypothetically result in damaging mechanical stress on the cardiovascular system. Therefore, the muscle function with a 10 kPa myocardium may provide the optimal combination of output and dependence of CO on HR, when compared to peristaltic pumping, while a more compliant myocardium lacks a sufficient output for any pumping function.

Impedance pumping is sensitive to operating conditions, mechanical properties, and geometrical properties [2]. The impedance pump function's inability to provide a sufficient CO and pressure is in conflict with the previous studies [2,5]. This conflict may be caused by low Reynolds number (0.11) and Womersley number (0.02) in zebrafish heart at this stage of development, when compared to the previous studies. In the zebrafish embryonic heart, viscous forces dominate, and pressure waves travel in phase with velocity waves. Therefore, irrespective of stiffness, pressure and CO was low in the current study of an impedance pumping function (Fig. 2.4b). The primary impact of stiffness is that pressure dampened out more quickly in the stiffer heart (Table. 2.2). The faster rate of dissipation for the less compliant wall agrees with theory, which is used to model the pressure outlet (Eq. 1). We acknowledge that an impedance pump is very sensitive to exact variations in stiffness along the pump and that we therefore may not be accurately depicting the intricacies of stiffness variations seen in an actual developing embryonic heart. With these limitations of an impedance pump it would restrict the robustness of operating conditions for the embryonic heart tube. Therefore, the current study indicates that the heart tube does not operate as an impedance pump, but the study also does not fully exclude the impedance pumping function as a possible function for driving blood flow for a heart tube, which is otherwise an intriguing pumping mechanism due to its efficiency. The peristaltic or muscle function pumping is more likely used by the embryonic heart over an impedance pump. However, any truly conclusive statement from a simulation would require very careful measurements in an experimental model – and these measurements are exceptionally challenging due to the small size of the heart.

Multiple limitations exist in the current study. Simulations assumed axisymmetric idealized geometry, despite the complex geometry and the dumbbell shaped compression of the lumen seen in actual hearts. As a first-order approximation, the myocardium and cardiac jelly are assumed Hookean, while residual stress and nonlinearities are neglected. The 2D imaging technique might cause some inaccuracy of the wall motion.

Cardiomyocytes are assumed to produce a constant force, while stiffness is applied uniformly along the entire heart tube for simulations, yet both force and stiffness could vary in an actual heart. Potentially the largest limitation in the current study, is that full contact between two solid walls during the contraction is not achieved in the FSI study, similar to several other publications [3,7,9,17]. Contact is not modeled due to the extreme technical challenges in performing an FSI with contact. In the FSI simulations, contact can lead to negative volumes in the mesh. Therefore, without contact, we may have more backflow than what could be occurring if contact was allowed. We also would have lower circumferential stress when compared to a model that includes contact. However, contact would come at the cost of tribological interactions between endocardial cells that could otherwise lead to cell damage and/or death. Therefore, we hypothesize that if contact occurs, it would not be at a very large compression force. Lastly, in experiments, plasma is assumed to have the same speed as red blood cells and that blood acts as a homogenous continuum. Overall, despite these limitations, the current study provided a better understanding of the mechanical properties and pumping efficiency in this stage of the embryonic heart development.

2.4 REFRENCES

1. Zhao, Y.; Srivastava, D. A Developmental View of MicroRNA Function. *Trends in biochemical sciences* **2007**, *32*, 189–197.
2. Avrahami, I.; Gharib, M. Computational Studies of Resonance Wave Pumping in Compliant Tubes. *Journal of Fluid Mechanics* **2008**, *608*, 139–160.
3. Forouhar, A.S.; Liebling, M.; Hickerson, A.; Nasiraei-Moghaddam, A.; Tsai, H.-J.; Hove, J.R.; Fraser, S.E.; Dickinson, M.E.; Gharib, M. The Embryonic Vertebrate Heart Tube Is a Dynamic Suction Pump. *Science* **2006**, *312*, 751–753.
4. Goenezen, S.; Rennie, M.Y.; Rugonyi, S. Biomechanics of Early Cardiac Development. *Biomechanics and modeling in mechanobiology* **2012**, *11*, 1187–1204.
5. Hickerson, A.I.; Gharib, M. On the Resonance of a Pliant Tube as a Mechanism for Valveless Pumping. *Journal of Fluid Mechanics* **2006**, *555*, 141.
6. Hickerson, A.I.; Rinderknecht, D.; Gharib, M. Experimental Study of the Behavior of a Valveless Impedance Pump. *Experiments in fluids* **2005**, *38*, 534–540.
7. Kozlovsky, P.; Bryson-Richardson, R.J.; Jaffa, A.J.; Rosenfeld, M.; Elad, D. The Driving Mechanism for Unidirectional Blood Flow in the Tubular Embryonic Heart. *Annals of biomedical engineering* **2016**, *44*, 3069–3083.
8. Männer, J.; Wessel, A.; Yelbuz, T.M. How Does the Tubular Embryonic Heart Work? Looking for the Physical Mechanism Generating Unidirectional Blood Flow in the Valveless Embryonic Heart Tube. *Developmental Dynamics* **2010**, *239*, 1035–1046.
9. Taber, L.A.; Zhang, J.; Perucchio, R. Computational Model for the Transition from Peristaltic to Pulsatile Flow in the Embryonic Heart Tube. **2007**.
10. Battista, N.A.; Lane, A.N.; Miller, L.A. On the dynamic suction pumping of blood cells in tubular hearts. In *Women in Mathematical Biology*; Springer, 2017; pp. 211–231.
11. Battista, N.A.; Miller, L.A. Bifurcations in Valveless Pumping Techniques from a Coupled Fluid-Structure-Electrophysiology Model in Heart Development. *arXiv preprint arXiv:1709.05264* **2017**.
12. Lee, J.; Moghadam, M.E.; Kung, E.; Cao, H.; Beebe, T.; Miller, Y.; Roman, B.L.; Lien, C.-L.; Chi, N.C.; Marsden, A.L. Moving Domain Computational Fluid Dynamics to Interface with an Embryonic Model of Cardiac Morphogenesis. *PloS one* **2013**, *8*, e72924.
13. Waldrop, L.; Miller, L. Large-Amplitude, Short-Wave Peristalsis and Its Implications for Transport. *Biomechanics and modeling in mechanobiology* **2016**, *15*, 629–642.
14. Rideout, V.C. *Mathematical and Computer Modeling of Physiological Systems*; Prentice Hall Englewood Cliffs, NJ:, 1991;
15. Schneider, C.A.; Rasband, W.S.; Eliceiri, K.W. NIH Image to ImageJ: 25 Years of Image Analysis. *Nature methods* **2012**, *9*, 671–675.
17. Loumes, L.; Avrahami, I.; Gharib, M. Resonant Pumping in a Multilayer Impedance Pump. *Physics of Fluids* **2008**, *20*, 023103.
18. Zamir, E.A.; Taber, L.A. Material Properties and Residual Stress in the Stage 12 Chick Heart during Cardiac Looping. *J. Biomech. Eng.* **2004**, *126*, 823–830.
19. Gendernalik, A.; Zebhi, B.; Ahuja, N.; Garrity, D.; Bark, D. In Vivo Pressurization of the Zebrafish Embryonic Heart as a Tool to Characterize Tissue Properties During Development. *Annals of Biomedical Engineering* **2020**, 1–12.

20. Bajaj, P.; Tang, X.; Saif, T.A.; Bashir, R. Stiffness of the Substrate Influences the Phenotype of Embryonic Chicken Cardiac Myocytes. *Journal of biomedical materials research Part A* **2010**, *95*, 1261–1269.
21. Bhana, B.; Iyer, R.K.; Chen, W.L.K.; Zhao, R.; Sider, K.L.; Likhitpanichkul, M.; Simmons, C.A.; Radisic, M. Influence of Substrate Stiffness on the Phenotype of Heart Cells. *Biotechnology and bioengineering* **2010**, *105*, 1148–1160.
22. Engler, A.J.; Carag-Krieger, C.; Johnson, C.P.; Raab, M.; Tang, H.-Y.; Speicher, D.W.; Sanger, J.W.; Sanger, J.M.; Discher, D.E. Embryonic Cardiomyocytes Beat Best on a Matrix with Heart-like Elasticity: Scar-like Rigidity Inhibits Beating. *Journal of cell science* **2008**, *121*, 3794–3802.
23. Jacot, J.G.; McCulloch, A.D.; Omens, J.H. Substrate Stiffness Affects the Functional Maturation of Neonatal Rat Ventricular Myocytes. *Biophysical journal* **2008**, *95*, 3479–3487.
24. Rodriguez, A.G.; Han, S.J.; Regnier, M.; Sniadecki, N.J. Substrate Stiffness Increases Twitch Power of Neonatal Cardiomyocytes in Correlation with Changes in Myofibril Structure and Intracellular Calcium. *Biophysical journal* **2011**, *101*, 2455–2464.
25. Edwards, J.N.; Blatter, L.A. Dysfunctional Intracellular Calcium Cycling in Cardiac Alternans. In Proceedings of the Proceedings of the Australian Physiological Society; 2013; Vol. 44, pp. 39–48.
26. Kimmel, C.B.; Ballard, W.W.; Kimmel, S.R.; Ullmann, B.; Schilling, T.F. Stages of Embryonic Development of the Zebrafish. *Developmental dynamics* **1995**, *203*, 253–310.
27. Johnson, B.M.; Garrity, D.M.; Dasi, L.P. The Transitional Cardiac Pumping Mechanics in the Embryonic Heart. *Cardiovascular engineering and technology* **2013**, *4*, 246–255.
28. Santhanakrishnan, A.; Miller, L.A. Fluid Dynamics of Heart Development. *Cell biochemistry and biophysics* **2011**, *61*, 1–22.
29. Taber, L.A.; Chabert, S. Theoretical and Experimental Study of Growth and Remodeling in the Developing Heart. *Biomechanics and modeling in mechanobiology* **2002**, *1*, 29–43.
30. Zamir, E.A.; Srinivasan, V.; Perucchio, R.; Taber, L.A. Mechanical Asymmetry in the Embryonic Chick Heart during Looping. *Annals of biomedical engineering* **2003**, *31*, 1327–1336.
31. Yoshigi, M.; Keller, B.B. Characterization of Embryonic Aortic Impedance with Lumped Parameter Models. *American Journal of Physiology-Heart and Circulatory Physiology* **1997**, *273*, H19–H27.
32. Bovo, E.; Dvornikov, A.V.; Mazurek, S.R.; de Tombe, P.P.; Zima, A.V. Mechanisms of Ca 2+ Handling in Zebrafish Ventricular Myocytes. *Pflügers Archiv-European Journal of Physiology* **2013**, *465*, 1775–1784.
33. De Vita, R.; Grange, R.; Nardinocchi, P.; Teresi, L. Mathematical Model for Isometric and Isotonic Muscle Contractions. *Journal of Theoretical Biology* **2017**, *425*, 1–10.
34. Yuryev, M.; Pellegrino, C.; Jokinen, V.; Andriichuk, L.; Khirug, S.; Khiroug, L.; Rivera, C. In Vivo Calcium Imaging of Evoked Calcium Waves in the Embryonic Cortex. *Frontiers in cellular neuroscience* **2016**, *9*, 500.
35. Abdul-Wajid, S.; Demarest, B.L.; Yost, H.J. *Loss of Embryonic Neural Crest Derived Cardiomyocytes Causes Adult Onset Hypertrophic Cardiomyopathy in Zebrafish. Nat Commun. 9: 1–11*; 2018;
36. Frank, O. Die Theorie Der Pulswellen. *Z Biol* **1926**, *85*, 91–130.

37. Malone, M.H.; Sciaky, N.; Stalheim, L.; Hahn, K.M.; Linney, E.; Johnson, G.L. Laser-Scanning Velocimetry: A Confocal Microscopy Method for Quantitative Measurement of Cardiovascular Performance in Zebrafish Embryos and Larvae. *BMC biotechnology* **2007**, *7*, 1–11.
38. Bark Jr, D.L.; Johnson, B.; Garrity, D.; Dasi, L.P. Valveless Pumping Mechanics of the Embryonic Heart during Cardiac Looping: Pressure and Flow through Micro-PIV. *Journal of biomechanics* **2017**, *50*, 50–55.
39. Hu, N.; Keller, B.B. Relationship of Simultaneous Atrial and Ventricular Pressures in Stage 16-27 Chick Embryos. *American Journal of Physiology-Heart and Circulatory Physiology* **1995**, *269*, H1359–H1362.
40. von Dassow, M.; Davidson, L.A. Natural Variation in Embryo Mechanics: Gastrulation in Xenopus Laevis Is Highly Robust to Variation in Tissue Stiffness. *Developmental dynamics: an official publication of the American Association of Anatomists* **2009**, *238*, 2–18.
41. Young, J.L.; Engler, A.J. Hydrogels with Time-Dependent Material Properties Enhance Cardiomyocyte Differentiation in Vitro. *Biomaterials* **2011**, *32*, 1002–1009.

CHAPTER 3- EFFECT OF FLOW MECHANICAL FORCES ON BLOOD CELLS

3.1 INTRODUCTION

von Willebrand Factor (VWF) is a multimeric protein involved in hemostasis (blood clotting) in arterial flow conditions. Although normally found in a globular form, VWF extends under specific flow conditions. VWF extension mediates platelet adhesion and rolling through its A1 domain. Similarly, exposure of its A2 domain allows for cleavage by A Disintegrin and Metalloproteinase with a Thrombospondin type-1 motif, member 13 (ADAMTS13) [1]. Cleavage of VWF leads to a decrease in hemostatic capacity, while excessive cleavage leads to acquired von Willebrand syndrome (aVWS), which impairs normal hemostasis. Our results show that the turbulent flow mediates VWF cleavage in the presence of ADAMTS13, decreasing the ability of VWF to sustain platelet adhesion. We have designed a serious of the experiments to study the effect of flow mechanical forces on VWF.

In the first study, we evaluate the effect and relative contributions of shear rate and elongational flow on VWF extension and cleavage by ADAMTS13. We developed three computational aortic valve models using patient Doppler echography data and calculated the shear rate and elongational flow present in normal, mildly stenotic, and severely stenotic aortic valves. We then developed microfluidic models to test the effects relevant shear rate and elongational flow on VWF cleavage by ADAMTS13.

The second one is rheometer as it has a rotor rotating inside a stator. This setup is similar to centrifuge pumps with different blade angels. We have studied fluid flow and VWF extension in different rotating speed. This study gives us understanding of the effect of rotating speed and mechanical forces on VWF.

In the third study, we investigate the flow patterns within a vortexer using three vortex speed settings and measured the rotational speed using a high-speed camera. We hypothesized that VWF cleavage is time-dependent and that turbulent flow at high vortex speeds can mediate cleavage by ADAMTS13 leading to structural and functional changes in VWF. This study shows the relation between turbulent forces and VWF cleavage although shear rate is smaller than the critical values.

And finally, we have used the polymer science theories to have a better understanding of VWF elongation and cleavage under different flow conditions. These findings impact the design of mechanical circulatory support devices and are relevant to pathological environments where turbulence is added to circulation.

3.2 METHOD

The VWF multimer study has been done with our colleagues in this project However, we explained the VWF multimer experimental method here. SDS-agarose gel electrophoresis was performed as previously described [8]. Briefly, low resolution gels (1.2%) were prepared (HGT agarose, Lonza, Rockland, ME), and 1 milliunit VWF from each sample was added to each lane. Electrophoresis was conducted for 16 h at 45 V. VWF multimers were then transferred to an Immobilon-P (Millipore, Billerica, MA) membrane at 4 °C in transfer buffer (25 mM Tris, 200 mM glycine, 20% methanol and 0.03% SDS). Western blotting and densitometry were performed on the gels as previously reported [9].

3.2.1 AORTIC VALVE AND MICROFLUIDIC DEVICE SIMULATION

The fluid in the aortic valves was assumed to be incompressible and Newtonian, with the latter commonly assumed in blood for high shear conditions [2,3]. Three aortic valve models were designed using patient data (Table 3.1): (a) healthy aortic valve, (b) mild stenosis and (c) severe stenosis. The aortic valves in the three cases were simulated as 2D axisymmetric models and the fluid flow. We note that this approach does not capture the geometry of the aortic sinus region. However, elongational flow (EF) and shear rate (SR) are relatively negligible in this region, which is why we use the simplified geometry. Geometry was based on patients with an aortic stenosis, where pressure drops were matched, while using a maximum sinus diameter of 1.24 cm and a leaflet length of 0.7 cm, a consistent choice for each model [4,5]. An inlet velocity condition was applied to match values during systole [2]. For all the simulations the pressure outlet equal to 0 Pa is applied, with no-slip boundary conditions at the walls.

To determine how the flow field may affect structures like VWF, we released massless particles at the inlet of the domain in a uniform distribution. Particles were released in every time step to assess the shear history of small-scale proteins like VWF.

Table 3.1: Aortic valve patient data and CFD model data

Patient	Aortic valve area (cm^2)	Max velocity (m/sec)	Mean Pressure gradient (mmHg)	Radius (cm)	Diameter (cm)
1	1	2.72	18.8	0.56	1.13
2	1.3	3.1	20.2	0.64	1.29
3	1.2	3.26	25.3	0.62	1.24
4	1.1	3.69	32.9	0.59	1.18
5	0.34	4.0	35	0.33	0.66
Healthy	4.4	0.6	3	1.18	2.36
Case1	2.2	2.23	17.5	0.83	1.66

Case2	1	3.45	38	0.56	1.12

The 2D axisymmetric simulations were conducted as for the aortic valve models with some modifications. The fluid in the channels was assumed to be incompressible and Newtonian [6,7]. Simulations and mesh generation were performed with ANSYS 18.1 (Pittsburgh, Pennsylvania, U.S.A.). A mesh sensitivity analysis was carried out to ensure that the numerical solutions are mesh independent with tetrahedral and triangular mesh elements totaling 100,000 elements for microchannel simulations and 50,000 for aortic valve simulations.

3.2.2 VANE RHEOMETER SIMULATION METHOD

The fluid in the vane-cylinder system is assumed incompressible and isothermal in the rotational speed. The fluid flow is governed by the three-dimensional, transient mass and momentum equations. The imposition of unsteadiness can significantly alter a flow, even resulting in partial or full relaminarization of an initially turbulent flow. Reynolds Stress Model (RSM-7 equations) was used. RSM may offer a more promising route towards accurately predicting transitional rotational flows, although at a greater computational cost than traditional turbulence models [8,9].

The 3D geometry comprising a four-bladed vane rotating in a cup were built and meshed by Ansys workbench software. The model is built based on the size and dimensions of FL16 4B/SS vane rotor and the CCB26 metal cup which are reported in table 3.2. A mesh sensitivity analysis was carried out to ensure that the numerical solutions are mesh independent. The mesh elements are mainly tetrahedral and triangular as well and in total 200000 elements have been used. The governing equations are solved by ANSYS-Fluent finite volume software. Numerical schemes were second order accurate. To make sure about the accuracy, results have been reported after reaching to residuals in the order of 10e-5.

Table 3.2: the geometrical specification of the rheometer

Radius of vane blades	8 mm
Height of the blades	8.8 mm
Blades thickness	1 mm
Axial gap between the vane blades and the bottom of the cup	1 mm
Inner radius of the cup	13.6 mm

No-slip boundary conditions were imposed on the solid surfaces. Blades are considered as solid surfaces rotating with angular velocity 4297 (1/min). The upper surface of the cup is considered as free surface.

3.2.3 SIMULATION METHOD OF VORTEX MIXER

Fluid in the cup was described by a dynamic mesh created in Ansys workbench and used in CFD package FLUENT. The flow regime involves a conical frustum dish of diameter 6.85 at the top and 6.35 at the bottom. The mean height of the fluid is 3.55 mm which is a third of the height of the dish. It is orbiting in an oval shape orbit with semi-major axis 4.6 mm and semi-minor axis 3.5 mm with three different speeds 180 rad/s, 112 rad/s and 34 rad/s. The whole mesh moves with the velocity imposed by the vortex mixer which was defined using an external C++ user-defined function (UDF) linked to FLUENT. Unsteady fluid motion in the orbiting cup was simulated with a multiphase volume of fluid (VOF) model in which the liquid–air interface share the same stress and velocity boundary conditions. Flow has been simulated turbulent and laminar based on the turbulent Reynolds number ($R_T = \frac{k^2}{\varepsilon \nu} \sim \frac{\nu_T}{\nu}$) and videos taken by high speed imaging technique.

No slip wall boundary conditions were applied to the entire dish model as in the experiment dish was with cap on. The gravitational force is also applied to consider the effect of gravity in fluid motion. Mesh independency studies show the number of grids with the best results is 80000 cells. Cells are finer near the wall with growth rate 1.2 and scalable wall function was used. For the turbulent simulation the Reynolds Stress Model (RSM-7 equations) was used. This model is suitable for complex 3D flows with strong streamline curvature, strong swirl/rotation [10]. The time step was 10e-6 (s) to have converged solution in each time step which is also chosen from time step independent study.

Reynolds number for rotating speeds 150 rad/s, 112 rad/s and 34 rad/s is approximately 2400, 1700, and 500. To have a better understanding of turbulent intensity in each rotating speed, turbulent Reynolds number for rotating speeds 150 rad/s, 112 rad/s and 34 rad/s are, 0.5, 50, and 250 respectively. As the turbulent Reynolds number for rotating speed 150 rad/s is two orders of magnitude larger than 35 rad/s, it is possible to conclude that the flow is turbulent as turbulent viscosity is significantly larger than molecular viscosity. It is concluded that the flow is laminar in rotating speed 35 rad/s, in transitional regime in 112 rad/s and turbulent in rotating speed 150 rad/s.

3.2.4 SCALING THEORY FOR CHAIN SESSION

In the current study, we are using theoretical drag force in laminar and flow regimes to calculate the tensile force applied to VWF and to study its extension and breakage in two flow regimes relative to reported experiments.

Based on a simple scaling theory for chain scission in laminar flow, the local fluid drag force is modeled with the following equation [27,33].

$$F_d \sim \chi \mu R^2 \quad (1)$$

μ is solvent viscosity, χ is principal strain rates and R is the polymer length scale, which is a function of the Deborah number (De). De is defined as the ratio of polymer (or multimer) relaxation time to flow residence time, and therefore defines how stretched VWF is likely to be.

De<<1, where chains are assumed fully stretched with R on the order of the VWF contour length. Contour length is the length at maximum possible extension which is equal to the product of the number of monomers and their length. R exhibits a large range that depends on multimer size from ~70 nm to 150 microns [34–36]. We note that ultra large multimers should not exist in plasma, except in pathological conditions.

Specifically, for De>>1, chains adopt a partially stretched conformation where R is approximated by the radius of gyration, estimated at 150 and 50 nm for VWF in an extended or coiled state respectively [37,38].Therefore, the force is inherently smaller when compared to Elongated VWF relaxation time is estimated on the order of 0.1s [39,40] ,while the flow residence time depends on specific flow conditions. Note that the impact of VWF rotation on the force is neglected in the current study, but it could impact upon the effective exposure time used to define the Deborah number since VWF in shear would experience cycling tension and compression along a specific axis, as opposed to sustained tension.

In turbulent flow the tensile drag force is conceptually set by the turbulent energy cascade[27],

$$F_d \sim \gamma \mu R^2 \quad (2)$$

where γ is the strain rate of velocity fluctuations associated with a specific spatial length scale (r), μ is the dynamic viscosity of the solvent, and *R* is the polymer length. γ is characterized based on 3 different categories. In the analysis, it is assumed that velocity fluctuations are on the order of the mean velocity, the largest eddy length scale is in the order of the characteristic length scale, and the Kolmogorov length scale is $\eta \sim dRe^{-3/4}$ [41]. By using the Taylor microscale formula ($r \sim (\frac{10\nu k}{\varepsilon})^{1/2}$), we can approximate γ. At the largest length scale, the strain rate is given by

$$\gamma \sim \frac{\mu Re_L}{\rho L^2}, \qquad (3)$$

where Re_L is Reynolds number which is based on the characteristic length scale of the flow, ρ is the density, and L is the characteristic length scale. In the inertial subrange ($\eta < r < L$),

$$\gamma \sim \frac{\mu Re_L}{\rho L^2} \left(\frac{r}{L}\right)^{-2/3}, \qquad (4)$$

where the strain rate increases as *r* decreases toward η which is the Kolmogorov length scale where energy is theoretically dissipated by viscosity. Once *r* decreases to the Kolmogorov length scale, the velocity gradient is assumed to be homogeneous and

$$\gamma \sim \frac{\mu Re_L^{3/2}}{\rho L^2}. \qquad (5)$$

3.3 RESULTS:

Using the Doppler echography data (Table 3.3), three CFD models of aortic valves were used to estimate the flow fields in aortic stenosis patients. As shown on Fig. 3.1a-c, CFD results show a systolic peak maximum flow velocity of 0.8 m/s in the healthy valve model, 2.5 m/s in a mild stenosis, and 3.5 m/s in a severe stenosis. The values for the mild and severe stenosis are comparable to those measured in AS patients (Table 3.4). EF along the leaflet (Fig. 3.1d-f) and SR (Fig. 3.1g-i) were calculated for each case throughout the flow domain and where these values are maximum, i.e. along the wall for the SR (Fig. 3.1j) and along the center of the channel for EF (Fig. 3.1k). These EF and SR values were used to design and inform flow rates in the fabrication of microfluidic devices.

Table 3.3. Particle Exposure Time: In the three aortic valve models

	Healthy Valve		Case 1: Aortic Stenosis		Case 2: Severe Aortic Stenosis	
Shear rate (1/s)	% particles	exposure time (ms)	% particles	exposure time (ms)	% particles	exposure time (ms)
0-1000	93.14	1-130	89.5	2-180	83.32	1-180
1000-5000	6.86	1-5	9.56	1-80	11.54	1-50
5000-10000	0	0	0.94	1-60	4.76	1-35
>10000	0	0	0	0	0.38	1-5

Table 3.4. Particle Exposure Time: Microfluidic models

	Hyperbolic Channel		90 Degree Channel	
$\dot{\gamma}(\frac{1}{s})$	% particles	exposure time (ms)	% particles	exposure time (ms)
0-1000	0.07	5-7	18.55	0.2-0.9
1000-5000	5.6	5-7	4.28	0.2-0.9
5000-10000	2.33	3-5	26.2	0.2-1
>10000	92	0.1-1	50.97	0.1-0.2

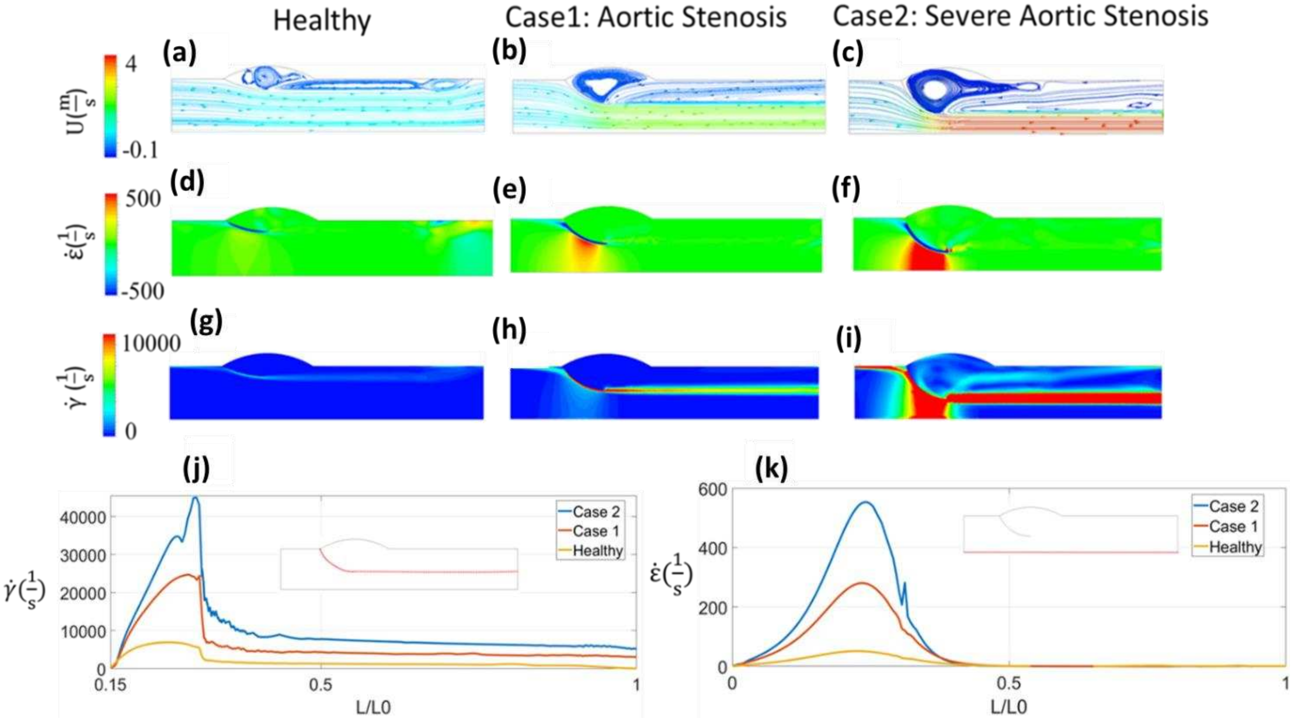

Figure 3.1. Computational Fluid Dynamics of three aortic valve models. Pathlines axial velocity (m/s), (a) Healthy Aortic Model (b) Case 1: Stenosis model (valve is 55% open) (c) Case 2: Severe aortic stenosis mode: (valve is 37% open). Elongational rate ($\dot{\varepsilon}$) (d) Healthy Aortic Model (e) Case 1 (f) Case 2. Shear Rate ($\dot{\gamma}$) (g) Healthy Aortic Model, (h) Case 1, (i) Case 2. Shear Rate ($\dot{\gamma}$) comparison (j) between case2, case1 and healthy on the leaflet and from leaflet to the outlet. Elongational rate ($\dot{\varepsilon}$) comparison (k) between case2, case1 and healthy on the centerline.

Two types of microfluidic devices were designed: (a) a hyperbolic function leading to a gradual constriction designed to increase the exposure time to the EF rates of interest present in severe AS (Fig. 3.2a) (b) a 90-degree angle to form a severe constriction and test the SR present in severe AS (Fig. 3.2b). CFD was conducted to calculate SR, EF, and velocity for flow rates of 10, 20, 30, 60, 140 and 250 µL/min within each microfluidic design (Fig. 3.2). Flow within the both microfluidic channels exhibit varying shear rates along the vertical and horizontal axis at each cross section (Fig. 3.2e-f). EF spikes at the inlet due to the gradual and constant cross-sectional change (Fig. 3.2g). This effect is not observed in the 90-degree channel because the channel cross section does not vary until the 90-degree angle construction is encountered.

In conclusion, the pathologic SR found from the severe AS CFD models were best tested at 140 μL/min in the 90-degree channel, while the EF in the found from the severe AS CFD models were best tested at 250 μL /min in the hyperbolic channel. However, various rates above and below these ranges were tested to fully evaluate the effects of SR and EF on VWF cleavage by ADAMTS13.

Table 3.5. Particle Exposure Time to Elongational Flow: In the three aortic valve models

	Healthy Valve		Case 1: Aortic Stenosis		Case 2: Severe Aortic Stenosis	
du/dx (1/s)	% particles	exposure time (ms)	% particles	exposure time (ms)	% particles	exposure time (ms)
<0	37.01	1-150	33.58	1-120	42.31	1-110
0-500	62.2	2-5	66.31	2-6	54.45	1-5
500-1000	0.79	1-3	0.098	1-4	3.24	1-3
>1000	0	0	0.01	1-3	0.047	1-3

Table 3.6. Particle Exposure Time to Elongational Flow: Microfluidic models

	Hyperbolic Channel		90 Degree Channel	
$\dot{\varepsilon}(\frac{1}{s})$	% particles	exposure time (ms)	% particles	exposure time (ms)
<0	49	1-7	46.19	0.1-1
0-500	33.15	1-3	52.03	0.2-0.6
500-1000	12.33	1-3	1.04	0.1-0.5
>1000	5.52	2-5	0.74	0.1-0.2

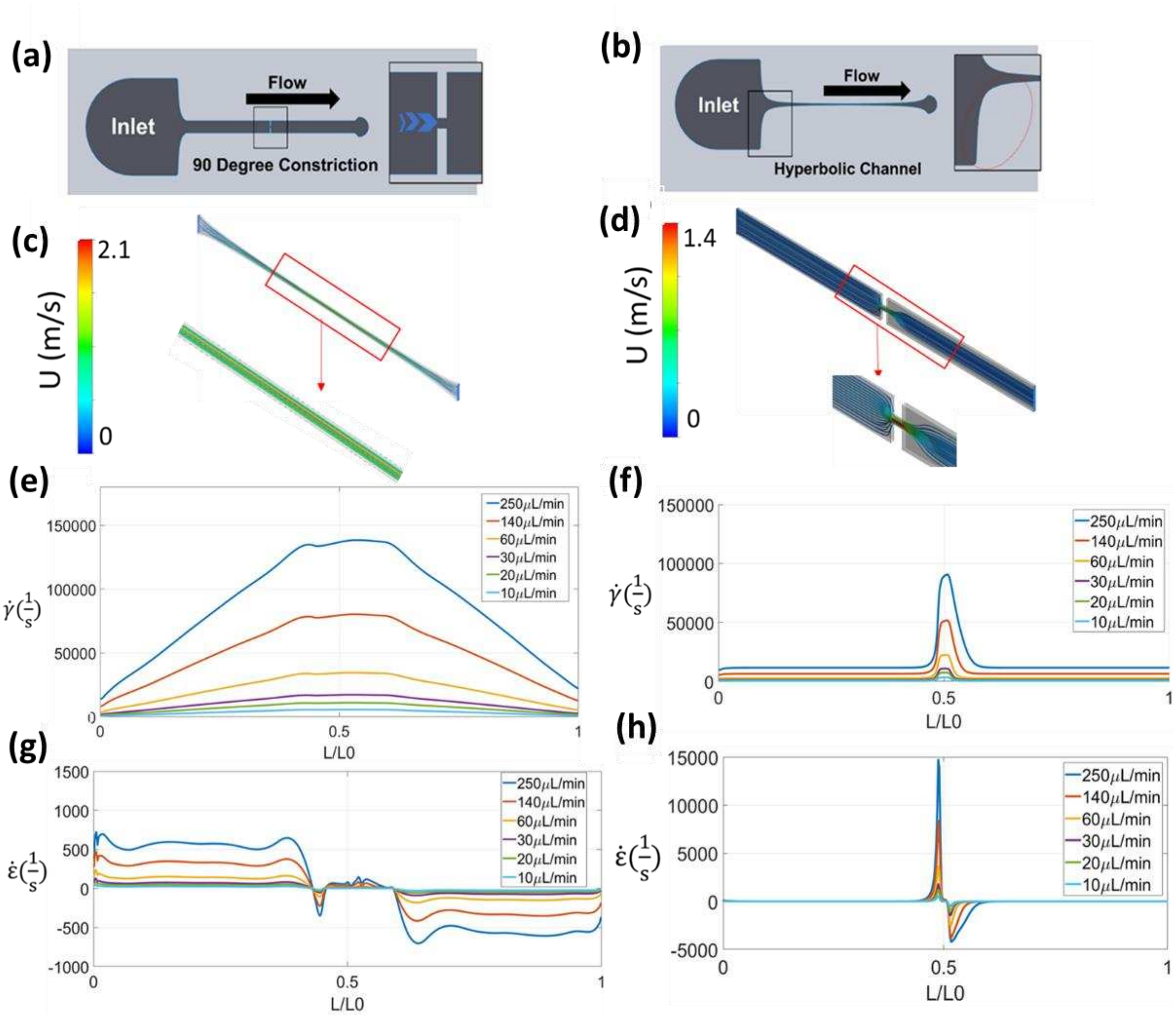

Figure 3.2. Microfluidic device designs and computational fluidic dynamics of the flow through the microfluidic channels**.** (a) Graphical representation of the 90 degree constriction (b) Graphical representation of the curved geometry described by hyperbolic function (c) Particle velocity through the 90 degree channel (stenosis) (d) Particle Velocity though the hyperbolic channel (e) Shear Rate ($\dot{\gamma}$) comparison in hyperbolic channel for different flowrates along the wall (f) Shear Rate ($\dot{\gamma}$) comparison in 90 degree channel for different flowrates along the wall (g) Elongational rate ($\dot{\varepsilon}$) comparison in hyperbolic channel for different flowrates on the centerline (h) Elongational rate ($\dot{\varepsilon}$) comparison in 90 degree channel for different flowrates on the centerline.

To identify the stresses the various VWF molecules might be exposed to in circulation in AS and in the microfluidic channels, we simulated massless particles. We then registered the percentage of particles exposed to various ranges of SR and EF along with the exposure times and used them to compare the aortic valve models with the microfluidic devices and the various inlet flow rates. Fig. 3.3a shows that when the VWF samples were tested in the 90-degree channel using an inlet flow rate of 140ul/min the percentage of particles exposed to the pathologic SR found in the severe AS encompassed values seen by the AS. Similarly, we found that the pathologic EF present in the severe AS cases was present in hyperbolic channel when tested at an inlet flow rate of 250 µL/min (Fig. 3.3b).

Since exposure time for a given stress will also affect cleavage of VWF by ADAMTS13 the corresponding exposure time for each condition was calculated. As shown in Tables 3.5 and 3.6, the exposure time to pathological SR (5000-10000, >100000) were comparable to that of the severe AS case at a flow rate of 140 µL/min (severe AS: 1-35 ms and 1-5 ms, 90 degree channel: 30-50, 0.5-2). In the case of EF, the exposure time to the pathologic EF (500-1000, >1000) was comparable to that of the severe AS case at a flow rate of 250 ul/min (severe AS: 1-3 ms and 1-3 ms, hyperbolic channel: 1-3, 2-5).

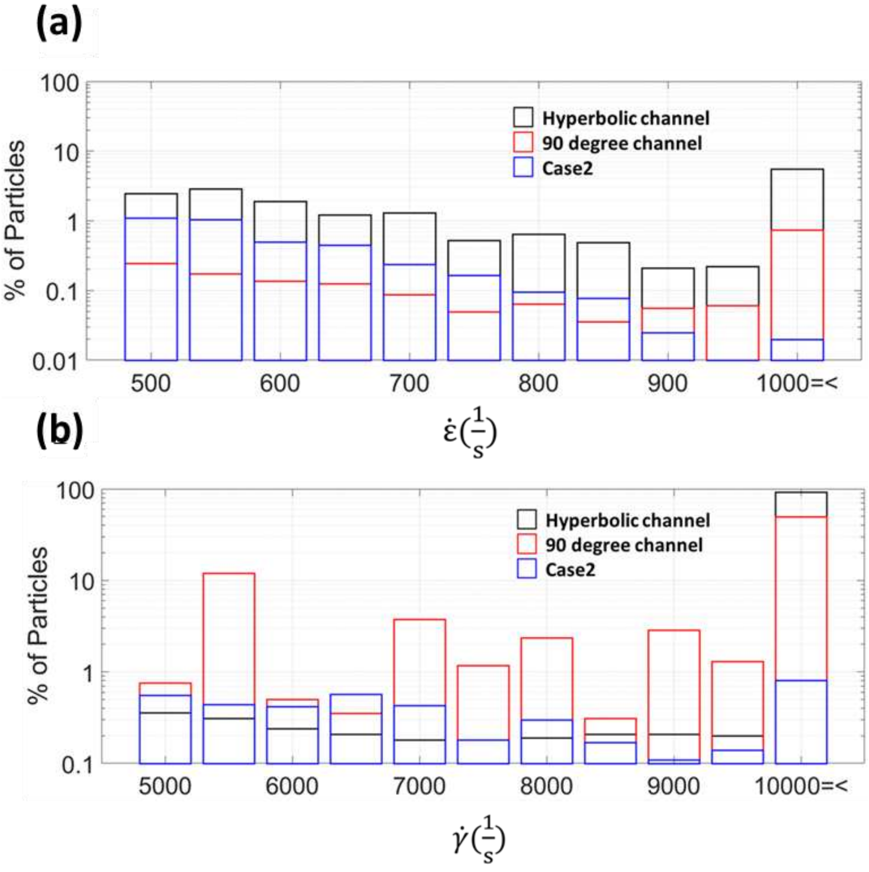

Figure 3.3. Comparison between Aortic valve models and Microfluidic Devices. (a) % Particle exposed to each Elongational rate ($\dot{\varepsilon}$) in the severe AS (Case 2) compared to the 90-degree channel (inlet flow rate: 250 µl/min) and Hyperbolic Channel (inlet flow rate: 250 µl/min). (b) % Particle exposed to each Shear Rate ($\dot{\gamma}$) in the severe AS (Case 2) compared to the 90-degree channel (inlet flow rate: 250 µl/min) and Hyperbolic Channel (inlet flow rate: 250 µl/min).

Based on the current results, high shear flow did not cause cleavage. Therefore, we have studied the effect of the turbulent flow on VWF degradation in the vane rheometer.

Fig. 3.4a-c shows the normalized spatial distribution of shear rate in three planes for each rotational rate. The maximum strain rate at the tip of the blade increases with rotational speed (Fig. 3.4d). For an increase in rotational speed, the maximum shear stress magnitude increases substantially (13-fold) from 10-100 rad/s, but only increases modestly (3.3-fold) from 100 to 450 rad/s, despite a larger change in rotational speed.

The Kolmogorov length scale is plotted in Fig. 3.4e. Energy from turbulence is completely dissipated by viscosity below this scale. As such, length scales below this value can be described through typical equations that define laminar flow. Note the relative size of the scale to plasma proteins and cells. The scale is not exact and is instead a theory grounded in the field of turbulence.

From the CFD model we found that as the rotational rate increases, so does the shear rate, with maximum values occurring near the vane (Fig. 3.4a-d). At a vane rotational rates 100 and 450 s^{-1}, the fluid shear rates have a maximum magnitude of 2000 and 6000 1/s adjacent to the surface of the vane. To test the hypothesis that turbulence, and not just high shear stress, is the cause of excessive VWF cleavage we conducted a set of experiments in a cone-and-plate rheometer under laminar flow conditions.

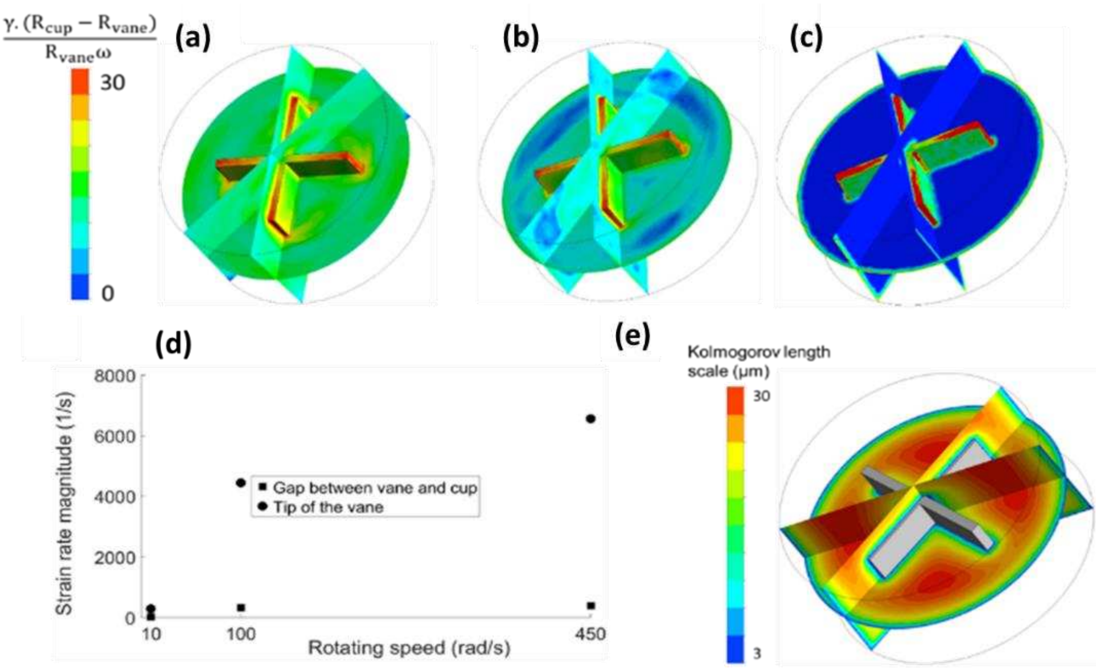

Figure 3.4: Normalized (velocity difference in the gap/gap width) strain rate (γ) for (a) 10 rad/s, (b) 100 rad/s, and (c) 450 rad/s. (d) Max shear stress at the tip of the blade and the gap between the blade and the cup for different rotating speeds, (e) Kolmogorov length scale for rotating speed 450 rad/s.

No cleavage was detected in samples exposed to laminar and transitional flow. Similarly, loss of HMWM of VWF was evident in the sample exposed to turbulent flow at both time points and interestingly, albeit less evident, in samples exposed to transitional flow (Fig. 3.5a) Cleavage was not observed on samples exposed to turbulent flow without ADAMTS13, indicating that cleavage was mediated by ADAMTS13 and not mechanical degradation. To investigate if the same cleavage occurs in the presence of blood cells and plasma, we performed experiments with whole blood. Whole blood samples subjected to turbulent conditions also showed loss of HMWM by multimer analysis (Fig. 3.5b). These data demonstrate that turbulent conditions in a vane rheometer are sufficient to cause VWF cleavage in the presence of ADAMTS13 in purified and whole blood systems. In the microchannel, samples were exposed to various flow rates within each channel. VWF cleavage by ADAMTS13 was not detected at any flow rate. Similarly, multimer analysis did not show loss of HMWM under any condition (Fig. 3.5c).

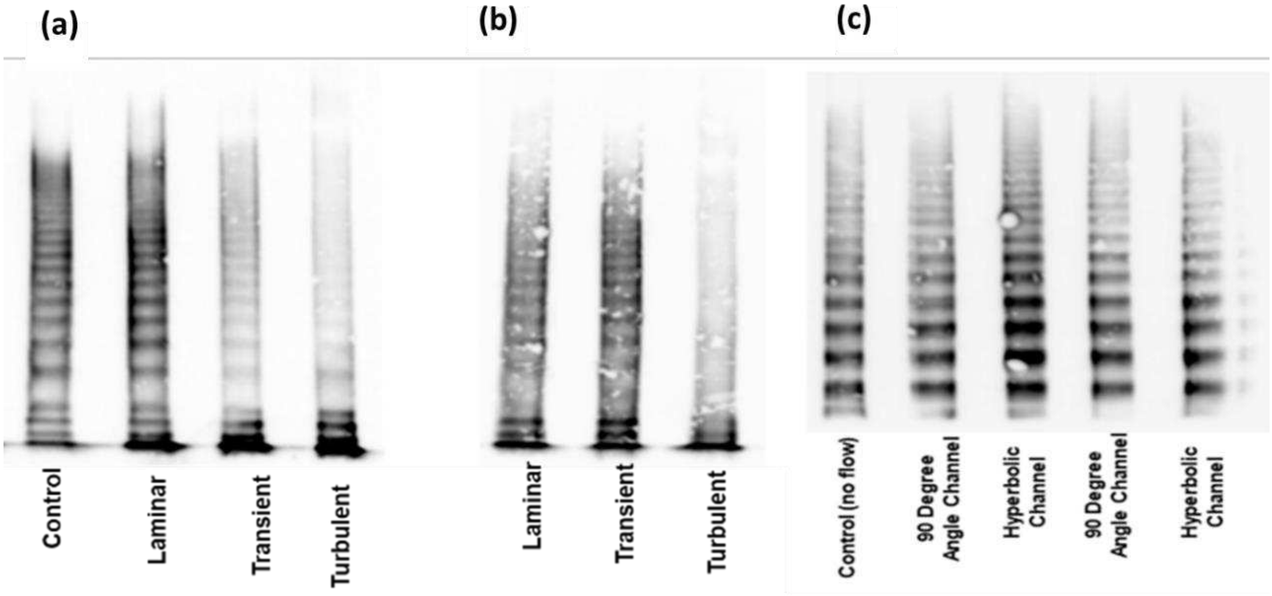

Figure 3.5: Effect of Elongational flow on VWF cleavage by ADAMTS13, (a) vane rheometer multimer analysis of samples exposed to CTRL: Unsheared sample, Laminar sample, Transitional sample and Turbulent conditions for 30 minutes (b) vane rheometer multimer analysis of blood samples tested. 1: Laminar flow, 2: Transitional flow, 3: Turbulent conditions, (c) microchannels representative Images of Multimer Analysis.

To look more into the effect of turbulent flow on VWF cleavage while the shear rate is not in the critical range, we have developed a model to simulate the flow behavior in a vortex mixer. We have validated our CFD results by using images obtained with a high-speed camera. The motion of the air-liquid interface agrees with the images obtained using high speed camera. The flow appears to decelerate in half of the orbit and then accelerates during the rest of the cycle. This change in speed happens thought the whole cycle due to elliptical orbit motion of the vortexed, which leads to a changing radius of curvature and therefore changing rotational velocity, i.e. acceleration or deceleration. At the lower rotational speed (35 rad/s) gravity forces are dominant and (liquid-air interface) exhibiting a slanted pattern associated with a balance of gravitational forces and forces caused by centripetal acceleration that act perpendicular to gravity. In the second setting, (rotational speed 112 rad/s) flow is raised all to the top of the well, such that it rotates as a bulk fluid around the wall of the well. However, viscous forces and gravity appear to determine the fluid motions as there is more fluid at the bottom of the well than at the top. Finally, at a setting of 7 (rotational speed 148 rad/s), the flow exhibits instabilities, but remains on the side wall of the well.

CFD results were verified using images obtained with a high-speed camera. As it is shown in Fig. 3.6a, the motion of the air-liquid interface agrees with the images obtained using high speed camera. The flow appears to decelerate as it travels from location 1 to 2 (Fig. 3.6a) and then accelerates from point 2 to 3 (Fig. 3.6a) due to the elliptical path created by the vortexer. This change in speed happens thought the whole cycle due to elliptical orbit motion of the vortexed, which leads to a changing radius of curvature and therefore changing rotational velocity, i.e. acceleration or deceleration. At a rotational speed of 35 rad/s gravity forces dominate the fluid behavior with the free surface (liquid-air interface) exhibiting a slanted pattern associated with a balance of gravitational forces and forces caused by centripetal acceleration that act perpendicular to gravity. In the second setting, (rotational speed 112 rad/s) flow is raised all to the top of the well, such that it rotates as a bulk fluid around the wall of the well. However, viscous forces and gravity appear to determine the fluid motions as there is more fluid at the bottom of the well than at the top. Finally, at a setting of 7 (rotational speed 148 rad/s), the flow exhibits instabilities, but remains on the side wall of the well, (Fig. 3.6a). In this setting inertial forces become significant and viscous and gravity forces are not dominant. Several vortices and irregularities are seen in the flow specially at point 2.

The CFD models were also used to evaluate shear rate magnitude (Fig. 3.6b) and wall shear stress (Fig. 3.6c) for each vortex setting and location within the well. These are both common parameters used to assess the potential for VWF elongation, as they can create extensional forces on VWF. The shear rate magnitude is a measure for the amount of stretch exhibited on fluid elements and therefore also on proteins in the flow. Wall shear stress (WSS), corresponds to where shearing stresses are typically highest, and these stresses have been reported to stretch VWF to aid in cleavage. Increasing the rotational speed increases the shear rate and WSS. The shear rate magnitude remains at or below 3000 s^{-1} for the highest rotational speed, while the WSS remains at or below 7 Pa.

Cleavage of VWF by ADAMTS13 was only detected after exposure to the highest vortex setting. The maximum shear rate present was $3000s^{-1}$, which was lower than the shear rates previously reported by other groups required for VWF cleavage [11]. These results suggest that shear rate alone might not be solely responsible for VWF extension and cleavage by ADAMTS13 under non-physiological conditions. Turbulent flow variables were also evaluated, as turbulence has been reported to contribute to “blood damage.” Turbulence leads to highly transient forces within the flow that can ultimately lead to very high instantaneous shear stress values that can’t be easily captured with the CFD approaches used here. The Kolmogorov scale and Reynolds Shea Stress (RSS) were evaluated for the vortex setting of 7 and 4.5. As shown on Figure 3.6a, only for a rotational speed of 148 rad/s does the Kolmogorov scale approach the size of VWF reported by prior authors [1,12]. The Kolmogorov scale is a theoretical spatial scale where energy from turbulent flow becomes dissipated by viscous forces. Similarly, the RSS is highest at a rotational speed of 148 rad/s and could be contributing to extension of VWF. RSS is commonly used to assess “blood damage” in turbulent flow.

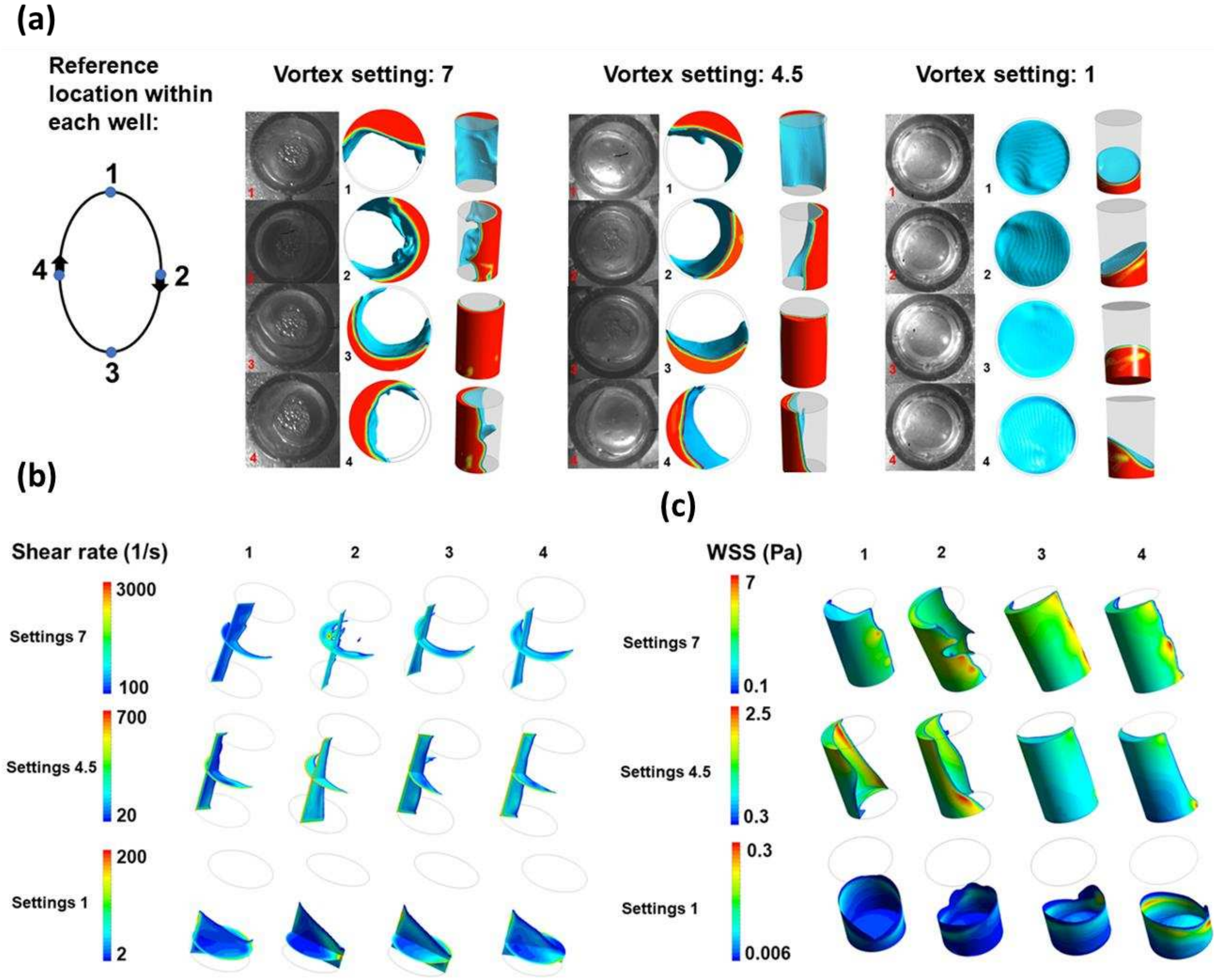

Figure 3.6. Vortex Flow CFD Model (a) Validation of CFD with images collected with a high-speed camera (b) Shear rate for each setting and location within the well (c) Wall shear stress for each setting and location within the well

The CFD models were also used to evaluate shear rate magnitude (Fig. 3.6) for each vortex setting and time period. Shear rate is a common parameter used to assess the potential for VWF elongation, as they can create extensional forces on VWF. The shear rate magnitude is a measure for stretch exhibited on fluid elements and therefore also on proteins in the flow. Increasing the rotational speed increases the fluid motion and consequently increases the shear rate. The shear rate magnitude remains at or below 5000 (s^{-1}) for the highest rotational speed which is smaller than the critical value reported for VWF cleavage [1].

The Kolmogorov scale was evaluated for the vortex setting of 7 and 4.5. As shown on Fig.3.7, only for a rotational speed of 148 rad/s does the Kolmogorov scale approach the size of VWF reported by prior authors [13]. The Kolmogorov scale is a theoretical spatial scale where energy from turbulent flow becomes dissipated by viscous forces.

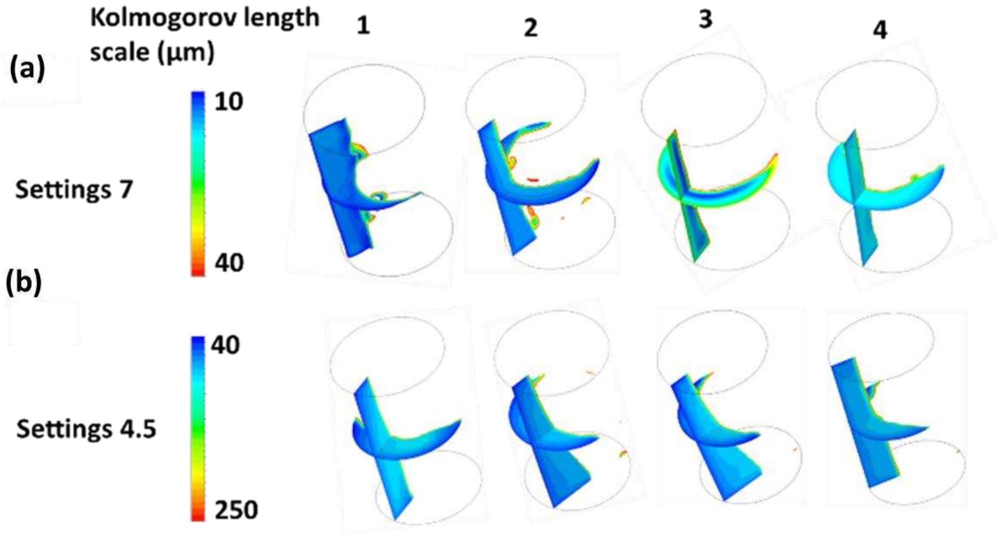

Figure 3.7: Kolmogorov length scale for (a) settings 7 (148 rad/s), and (b) settings 4.5 (112 rad/s)

Since the Kolmogorov scale is a theoretical scale where energy from turbulent flow becomes dissipated by viscous forces, this is also a theoretical scale where transient effects associated with turbulent flow may become relatively satisfied, meaning that VWF at a larger scale would experience very large transient forces, while VWF at smaller scales may experience viscous forces more typical of laminar flow. Turbulence is a complex topic that is not fully understood, especially at small scales and the Kolmogorov scale is only a theoretical scale. As we have previously reported, there are smaller scales that can also experience very large instantaneous shear stress values.

The fluid conditions commonly described as pathologic that lead to excessive breakage of VWF have not been fully characterized, although are hypothesized in the field to involve either high shear stress or elongational flow since these flow conditions are thought to lead to VWF extension [14,15].

The effect of elongational flow and shear rate on VWF cleavage has considered in several studies, with the latter consisting of both an extensional (principal stresses) and rotational component [16–21]. Simulations using a worm-like chain model demonstrate a globule-stretch transition near a shear rate of 5,000 s^{-1}, as shear forces in the flow create tension on the polymer, or multimer in this case, and extends it [22]. More recent studies have demonstrated that turbulent flow conditions may be fundamental to exacerbating VWF cleavage [13,23]. This could be due to increased mixing, collisions, high instantaneous shear stress, or through the interaction of turbulent eddies. To dissect out the processes leading to cleavage for turbulent flow, there remains a need to quantify the fluid forces relative to forces expected in laminar flow in relation to VWF cleavage.

Polymer chains can be cleaved by mechanical forces in both laminar and turbulent flow with further modulation through the local chemical environment. Mechanically induced scission, such as the one caused by strong extensional flows, has been studied experimentally since the early seventies[24–26]. Scission theories for laminar and turbulent flow hypothesize that the drag force experienced by the chain makes sufficient tension to break the chain if it is larger than the critical strength of a polymer covalent bond [27]. The assumption in laminar extensional flow is the maximum tension is at the midpoint [28]. A certain wall shear stress [29,30]or strain rate [31] is necessary to have a randomly coiled polymer extend prior to this breakage. This is the onset phenomenon. In predicting the onset phenomenon, researchers propose both length scale and time scale models. For the laminar flow, in the length scale model, the strain rate is related to the polymer chain length. In the time scale model, the onset occurs when the time ratio of polymer relaxation time to flow residence time (or Deborah number) is around unity. For the turbulent flow, onset occurs in the length scale model when the ratio of the polymer length scale (radius of gyration) to the turbulent length scale reaches a certain value. Many studies have preferred the time scale model because the polymer size is several orders of magnitude smaller than the turbulent eddy size at onset, while the polymer relaxation time is about the same order as the turbulent time scale [29–32].

Since VWF is a multimer that has many similar features to a polymer, we are extending polymeric scission theories and utilizing them to study VWF behavior in different flow regimes. This can improve our understanding of where and how VWF stretch can occur in relation to cleavage with a systematic mathematical approach. To do that, we have designed a study to investigate the VWF extension and breakage in different flow regimes by calculating the fluid forces that may work synergistically with ADAMTS13 to support cleavage.

Table 3.7 summarizes the previous studies focused on VWF extension or cleavage in experiments from the literature. Data provided in the table 3.7 parameterizes calculations for equations 1-5 and is used to compare experimental VWF elongation and/or cleavage to predictions of theoretical force.

Table 3.7. Parameters found in experimental studies where, NM: Not measured, N/A: Not applicable, χ: principal strain rate, γ: turbulent flow strain rate, η: Kolmogorov length scale, t_e: exposure time.

Case	Flow regime	γ, χ (1/s)	η (μm)	$t_e(s)$	extended	unfolded	Cleaved	Ref

1	Laminar	200-3,000	N/A	0.2-0.5	NM	NM	No	[13,23]
2	Laminar	4,000-5,000	N/A	NM	Yes	Yes	No	[42]
3	Laminar	10,000	N/A	1,200-8,400	NM	NM	Yes	[42]
4	Laminar	5,000-10,000	N/A	0.1-0.3	Yes	Yes	NM	[14]
5	Laminar	200-130,000	N/A	0.001-0.1	NM	NM	No	[23]
6	Turbulent	2,000-6,000	10-40	0.0002-0.001	NM	NM	Yes	[13]
7	Turbulent	5,000-10,000	20-35	0.0001-0.001	NM	NM	Yes	[23]
8	Turbulent	300,000	NM	10	NM	NM	Yes	[43]

Here we are studying the drag force effect on VWF in laminar flow. Note that multimer size can vary substantially in a blood sample, from 500 kDa for a dimer with an estimated contour length of ~140 nm to >10,000 kDa for high molecular weight multimers found in plasma, corresponding to a contour length of >2.8 µm. N-terminal fragments can be as small as 140 kDa. However, the impact of VWF cleavage on hemostatic capacity occurs with the loss of high molecular weight multimers (>~1.5 µm). With this range, the applied extensional force in laminar flow escalates with increasing contour length for De<<1 which is shown in Fig. 3.8, as flow residence time exceeds polymer relaxation time (~0.1s). Forces to achieve extension decrease with contour length, meaning that the highest molecular weight multimers are most likely to extend. Based on Eq. 1, this would occur for contour lengths above 6.3 μm[44]. To also unfold the A2 domain, 10-22 pN [10,45,46] of tension must exist locally across the domain, which is expected to occur near the multimer center. In addition, the average lifetime of VWF and ADAMTS13 bonds is maximized at 22 pN [47]. For high 10,000 kDa multimers, cleavage is only expected when shear rates exceed 10,000 s^{-1}. Increasing the contour length to 15 μm, requires a lower strain rate of 100-1000 s^{-1} for optimized A2 unfolding. Therefore, the largest multimers experience the highest tensile force across A2, while cleavage to a smaller size leads to less chance for additional cleavage of less hemostatically active VWF multimers. These results do not preclude cleavage at lower shear rates since rupture/cleavage can still occur at lower tensile forces (<20 pN) if enough time is given, just with less probability[10]. Overall, the combination of exposure time, shear rate, and multimer size leads to cleavage, as in agreement with Lippok et al [42]. For laminar flow, cases 1-4 exhibit a De<<1, which shows the possibility of the VWF unfolding. In conclusion the risk of cleavage in laminar flow is low if the strain rate is not in the order of 100,000 or the exposure time is not larger than 600-1200 seconds [42]which is not a physiological condition.

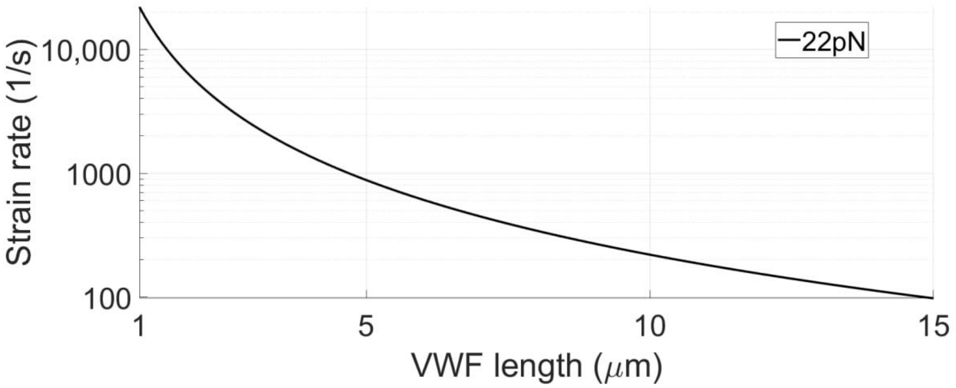

Figure 3.8. Force applied to VWF in laminar flow for a Deborah number much smaller than 1.

Instead of De<<1, De>>1 exhibits much lower drag force values, as shown in Fig. 3.9 for large range of strain rate. The maximum drag force for De>>1 is larger than the critical force to unfold the VWF but its far beyond the critical force for cleavage. VWF in Case 5 (Table.3.7) experience a drag force larger than 0.4 pN, which is enough force for the unfold VWF. Based on these results, extension, or cleavage of VWF is unlikely when flow for De>>1, which means that VWF would need to be in extended state to achieve sufficient tension for extension, which is in agreement with the literature[35].

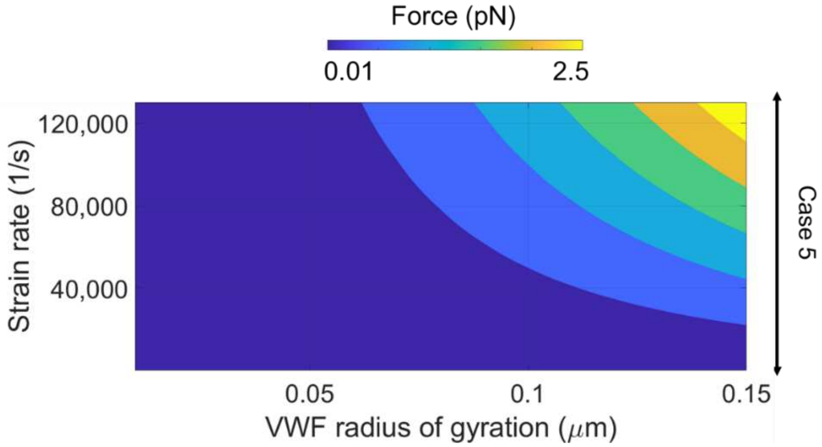

Figure 3.9. Force applied to VWF in laminar flow when the Deborah Number is much larger than 1.

Turbulent flow is also considered since laminar flow is unlikely to lead to cleavage based on the above arguments, except in very extreme conditions involving either very high shear rates, Fig. 3.7, or very long (non-physiological) exposure times [42]. Based on experimental studies demonstrating cleavage in turbulent flow in Table.3.7 [13,23], the spatial inertia scale (r) is in the range of 100 to 900 m . The Kolmogorov length scale (η) is in the range of 3 to 40 μm. The drag forces when the spatial scale is equal to the characteristic length scale are shown in Fig. 3.10a. The drag force is not large enough to cause unfolding or cleavage of the VWF. Drag forces for the turbulent inertial range (η< r< d) are shown in Fig. 3.10b. The drag force increases with VWF contour length, similar to laminar flow. However, the drag force achieved for a given contour length is much higher in turbulent flow, with the largest molecular weight multimers receiving the highest tensile force. When the spatial length scale gets close to the smallest value of 100 μm, the drag force is the largest, meaning that the smallest eddies have the largest impact on VWF extension and domain unfolding. Conceptually interactions between the smallest eddies would create large local transient forces, while large eddies entrain VWF without the large fluctuations seen at the smaller scales. A region of 10-22 pN is highlighted in the figure to show a threshold of where cleavage is expected. As the inertial scale decreases down to the Kolmogorov length scale, the drag force becomes very large, Fig. 3.10c. High molecular weight multimers (>1.5 μm) have a high probability for cleavage at this scale based on the force magnitude, which is in agreement with the literature, Table 3.7 [23]. Energy from turbulence at this scale would be absorbed by viscosity, as well as protein and cell deformation.

We hypothesize that in the inertial and Kolmogorov length scales, VWF cleavage does not require a 2-step process of 1) extension and 2) domain unfolding. Instead, intriguingly, a concentration of high intermittent stress could occur at many points around VWF in a globular state, as opposed to a single point at the center of extended VWF in suspension, making cleavage much more efficient[44]. Comparatively, even for shear rates of 5,000 s^{-1}, substantial loss of high molecular weight multimers is seen in experiments within minutes for turbulent flow, compared to a time scale of hours for laminar flow [13,42]. It is noted that the analysis does not account for intermittency and shear stress fluctuations, which can otherwise significantly enhance instantaneous tensile forces [48]. In conclusion, a large Reynolds number (Re_L), leading to turbulence could increase the probability for the loss of high molecular weight VWF multimers.

Furthermore, higher Re_L leads to smaller scale turbulent structure, which should lead to increased extensional force, as shown in Fig. 3.10.

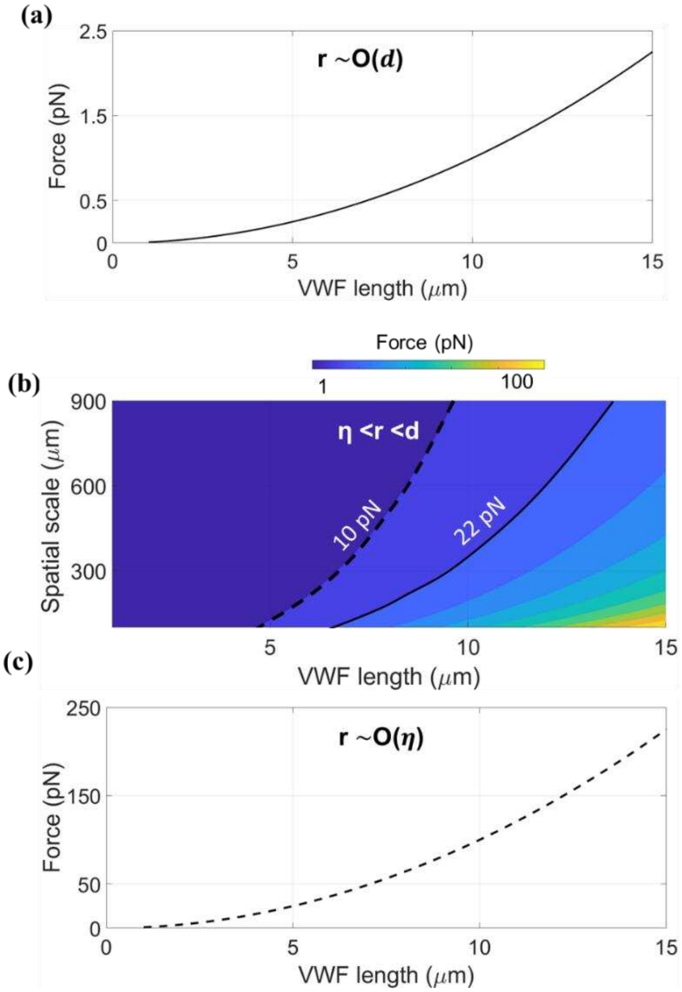

Figure 3.10. Force applied to VWF in the turbulent flow for different VWF contour length and spatial scale of (a) largest length scale r $\sim$O(d), (b) the inertial range (η< r< d), the critical force for unfolding is in the range of 10-22 pN (c) the smallest length scale r $\sim$O(η).

Overall, we have summarized our hypothesis and findings in Fig. 3.11. VWF extension, where De<<1, is required to obtain sufficient forces for domain unfolding and cleavage. However, laminar flow is inefficient at cleaving high molecular weight multimers because it cleaves at a single region in the center of an extended multimer, where tension is highest, and the probability for cleavage is expected to only be high at very high shear rates, thereby requiring sustained exposure for low or moderate shear in order to see cleavage[42]. The highest molecular weight multimers experience the highest tensile forces, thereby exposing the largest region where A2 unfolding is expected, while smaller multimers may not have efficient cleavage due to lower expected forces. Without very high shear or nonphysiological exposure times, cleavage is only expected in laminar flow [19,20]. Alternatively, for turbulent flow, interacting eddies might lead to cleavage at multiple site, while VWF remains in a globular form, regardless of the local shear rate, which is in agreement with experiments [19]. In turbulent flow, primary parameters that can influence VWF A2 unfolding, include the Reynolds number and multimer size. As the Reynolds number increases, there is an increased amount of turbulent structures, with smaller scale structures. The current work demonstrates that the smallest scale turbulent structures have the biggest effect on tensile forces within VWF. Overall, turbulent flow is expected to lead to efficient cleavage of VWF when compared to laminar flow due to high spatially disperse extensional forces.

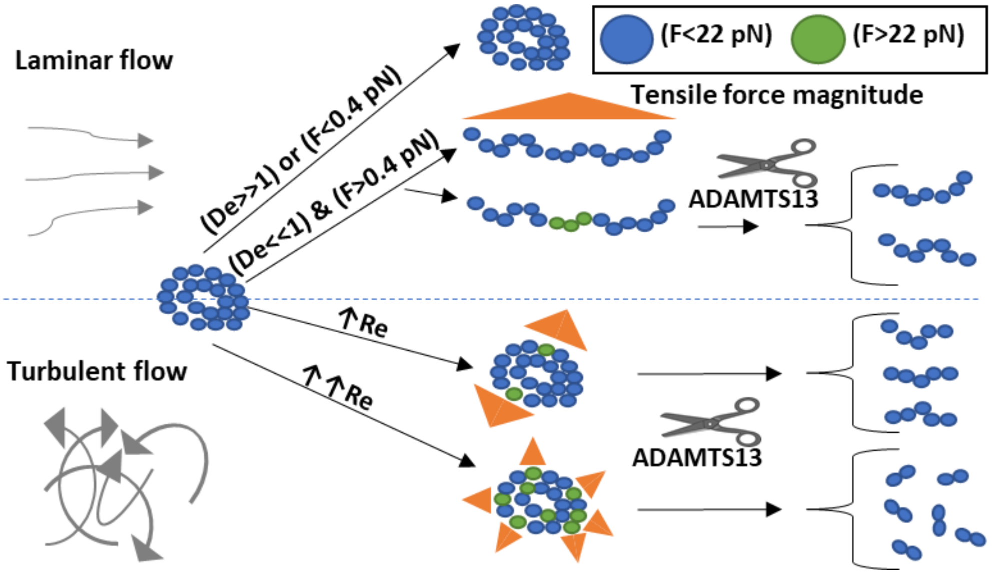

Fig. 3.11: Hypothetical drawing of the VWF stretch and cleavage in (a) laminar flow (b) turbulent flow.

There are several assumptions in the current study. The calculated drag force is an approximation for both the laminar and turbulent flow. For laminar flow, the exact tensile force would depend on the instantaneous orientation of VWF relative to principal stresses, would depend on rotation, and specific shapes or conformations. In calculated the De number, the exposure time is highly simplified, whereas VWF extension likely depends on the type of flow, i.e. shear vs. elongational flow. This is because rotation of VWF in flow typical of shear flow would cycle VWF through compressive and tensile states, whereas elongational flow would create sustained tensile forces along a single direction. For turbulent flow, the actual tensile force and distribution of tensile forces along a VWF multimer remains theoretical. The theories used in this study do not account for effects from a solid wall. We assume homogeneous and isotropic turbulence. There is no calculation for the transitional flow regime that might exist in some of the cited experiments. Lastly, polymer scission theories are being applied to biological multimers, which can otherwise experience different behaviors, such as self-association.

Scission theory, developed for polymers, has been applied to study theoretical forces that could exist across the A2 domain of VWF in a suspension of fluid. Calculations combined with experimental observations from the literature demonstrate how several flow parameters can impact upon VWF cleavage. In laminar flow, either non-realistically high shear rates or exposure times are needed to see cleavage based on the theory. However, in the turbulent flow, large tensile forces are expected in VWF, regardless of prior extension. These tensile forces are primarily dominated by small turbulent structures near or at the Kolmogorov scale.

3.4 REFERENCES

1. Springer, T.A. Von Willebrand Factor, Jedi Knight of the Bloodstream. *Blood* **2014**, *124*, 1412–1425.
2. Amindari, A.; Saltik, L.; Kirkkopru, K.; Yacoub, M.; Yalcin, H.C. Assessment of Calcified Aortic Valve Leaflet Deformations and Blood Flow Dynamics Using Fluid-Structure Interaction Modeling. *Informatics in Medicine Unlocked* **2017**, *9*, 191–199.
3. Chandra, S.; Rajamannan, N.M.; Sucosky, P. Computational Assessment of Bicuspid Aortic Valve Wall-Shear Stress: Implications for Calcific Aortic Valve Disease. *Biomechanics and modeling in mechanobiology* **2012**, *11*, 1085–1096.
4. Marom, G.; Rotman, O.M.; Slepian, M.J.; Prabhakar, S.; Horner, M. Ram P. Ghosh 7. *Mechanics* **2018**, *5*, 6.
5. Ghosh, R.P.; Marom, G.; Rotman, O.M.; Slepian, M.J.; Prabhakar, S.; Horner, M.; Bluestein, D. Comparative Fluid–Structure Interaction Analysis of Polymeric Transcatheter and Surgical Aortic Valves' Hemodynamics and Structural Mechanics. *Journal of biomechanical engineering* **2018**, *140*.
6. Amindari, A.; Saltik, L.; Kirkkopru, K.; Yacoub, M.; Yalcin, H.C. Assessment of Calcified Aortic Valve Leaflet Deformations and Blood Flow Dynamics Using Fluid-Structure Interaction Modeling. *Informatics in Medicine Unlocked* **2017**, *9*, 191–199, doi:https://doi.org/10.1016/j.imu.2017.09.001.
7. Chandra, S.; Rajamannan, N.M.; Sucosky, P. Computational Assessment of Bicuspid Aortic Valve Wall-Shear Stress: Implications for Calcific Aortic Valve Disease. *Biomechanics and Modeling in Mechanobiology* **2012**, *11*, 1085–1096, doi:10.1007/s10237-012-0375-x.
8. De Tullio, M.D.; Afferrante, L.; Demelio, G.; Pascazio, G.; Verzicco, R. Fluid–Structure Interaction of Deformable Aortic Prostheses with a Bileaflet Mechanical Valve. *Journal of biomechanics* **2011**, *44*, 1684–1690.
9. Ge, L.; Leo, H.-L.; Sotiropoulos, F.; Yoganathan, A.P. Flow in a Mechanical Bileaflet Heart Valve at Laminar and Near-Peak Systole Flow Rates: CFD Simulations and Experiments. **2005**.
10. Wu, T.; Lin, J.; Cruz, M.A.; Dong, J.; Zhu, C. Force-Induced Cleavage of Single VWFA1A2A3 Tridomains by ADAMTS-13. *Blood* **2010**, *115*, 370–378, doi:10.1182/blood-2009-03-210369.
11. Shankaran, H.; Alexandridis, P.; Neelamegham, S. Aspects of Hydrodynamic Shear Regulating Shear-Induced Platelet Activation and Self-Association of von Willebrand Factor in Suspension. *Blood, The Journal of the American Society of Hematology* **2003**, *101*, 2637–2645.
12. DONG, J.-F. Cleavage of Ultra-Large von Willebrand Factor by ADAMTS-13 under Flow Conditions. *Journal of Thrombosis and Haemostasis* **2005**, *3*, 1710–1716, doi:10.1111/j.1538-7836.2005.01360.x.
13. Bortot, M.; Ashworth, K.; Sharifi, A.; Walker, F.; Crawford, N.C.; Neeves, K.B.; Bark Jr, D.; Di Paola, J. Turbulent Flow Promotes Cleavage of VWF (von Willebrand Factor) by ADAMTS13 (a Disintegrin and Metalloproteinase with a Thrombospondin Type-1 Motif, Member 13). *Arteriosclerosis, thrombosis, and vascular biology* **2019**, *39*, 1831–1842.

14. Schneider, S.W.; Nuschele, S.; Wixforth, A.; Gorzelanny, C.; Alexander-Katz, A.; Netz, R.R.; Schneider, M.F. Shear-Induced Unfolding Triggers Adhesion of von Willebrand Factor Fibers. *Proceedings of the National Academy of Sciences* **2007**, *104*, 7899–7903.
15. Sing, C.E.; Alexander-Katz, A. Elongational Flow Induces the Unfolding of von Willebrand Factor at Physiological Flow Rates. *Biophysical journal* **2010**, *98*, L35–L37.
16. Doyle, P.S.; Shaqfeh, E.S. Dynamic Simulation of Freely-Draining, Flexible Bead-Rod Chains: Start-up of Extensional and Shear Flow. *Journal of non-newtonian fluid mechanics* **1998**, *76*, 43–78.
17. Alexander-Katz, A.; Netz, R.R. Dynamics and Instabilities of Collapsed Polymers in Shear Flow. *Macromolecules* **2008**, *41*, 3363–3374.
18. Sunthar, P.; Nguyen, D.A.; Dubbelboer, R.; Prakash, J.R.; Sridhar, T. Measurement and Prediction of the Elongational Stress Growth in a Dilute Solution of DNA Molecules. *Macromolecules* **2005**, *38*, 10200–10209.
19. Neelov, I.M.; Adolf, D.B.; Lyulin, A.V.; Davies, G.R. Brownian Dynamics Simulation of Linear Polymers under Elongational Flow: Bead–Rod Model with Hydrodynamic Interactions. *The Journal of chemical physics* **2002**, *117*, 4030–4041.
20. Venkataramani, V.; Sureshkumar, R.; Khomami, B. Coarse-Grained Modeling of Macromolecular Solutions Using a Configuration-Based Approach. *Journal of Rheology* **2008**, *52*, 1143–1177.
21. Harrison, G.M.; Remmelgas, J.; Leal, L.G. The Dynamics of Ultradilute Polymer Solutions in Transient Flow: Comparison of Dumbbell-Based Theory and Experiment. *Journal of Rheology* **1998**, *42*, 1039–1058.
22. Alexander-Katz, A.; Schneider, M.F.; Schneider, S.W.; Wixforth, A.; Netz, R.R. Shear-Flow-Induced Unfolding of Polymeric Globules. *Physical review letters* **2006**, *97*, 138101.
23. Bortot, M.; Sharifi, A.; Ashworth, K.; Walker, F.; Cox, A.; Ruegg, K.; Clendenen, N.; Neeves, K.B.; Bark, D.; Di Paola, J. Pathologic Shear and Elongation Rates Do Not Cause Cleavage of Von Willebrand Factor by ADAMTS13 in a Purified System. *Cellular and Molecular Bioengineering* **2020**, *13*, 379–390.
24. Horn, A.F.; Merrill, E.W. Midpoint Scission of Macromolecules in Dilute Solution in Turbulent Flow. *Nature* **1984**, *312*, 140–141, doi:10.1038/312140a0.
25. Keller, A.; Odell, J.A. The Extensibility of Macromolecules in Solution; A New Focus for Macromolecular Science. *Colloid & Polymer Sci* **1985**, *263*, 181–201, doi:10.1007/BF01415506.
26. Nguyen, T.Q.; Kausch, H.-H. Chain Scission in Transient Extensional Flow Kinetics and Molecular Weight Dependence. *Journal of Non-Newtonian Fluid Mechanics* **1988**, *30*, 125–140, doi:10.1016/0377-0257(88)85020-1.
27. Universal Scaling for Polymer Chain Scission in Turbulence | PNAS Available online: https://www.pnas.org/content/103/45/16660.short (accessed on 23 November 2020).
28. Perkins, T.T.; Smith, D.E.; Chu, S. Single Polymer Dynamics in an Elongational Flow. *Science* **1997**, *276*, 2016–2021, doi:10.1126/science.276.5321.2016.
29. Drag Reduction Fundamentals - Virk - 1975 - AIChE Journal - Wiley Online Library Available online: https://aiche.onlinelibrary.wiley.com/doi/abs/10.1002/aic.690210402?casa_token=URnE3nKXNBkAAAAA:eSiXageo-olThvJFFEA_cy_Jr-nJKekdnKjiS6SXX7suJtIQSOXv-fT-oQllup_O2WTbgwLrI5AdMcY (accessed on 23 November 2020).

30. Gold, P.I.; Amar, P.K.; Swaidan, B.E. Friction Reduction Degradation in Dilute Poly(Ethylene Oxide) Solutions. *Journal of Applied Polymer Science* **1973**, *17*, 333–350, doi:https://doi.org/10.1002/app.1973.070170202.
31. Hershey, H.C.; Zakin, J.L. A Molecular Approach to Predicting the Onset of Drag Reduction in the Turbulent Flow of Dilute Polymer Solutions. *Chemical Engineering Science* **1967**, *22*, 1847–1857, doi:10.1016/0009-2509(67)80215-X.
32. Virk, P.S.; Merrill, E.W. The Onset of Dilute Polymer Solution Phenomena. In Proceedings of the Viscous Drag Reduction; Wells, C.S., Ed.; Springer US: Boston, MA, 1969; pp. 107–130.
33. Odell, J.A.; Keller, A. Flow-Induced Chain Fracture of Isolated Linear Macromolecules in Solution. *Journal of Polymer Science Part B: Polymer Physics* **1986**, *24*, 1889–1916, doi:https://doi.org/10.1002/polb.1986.090240901.
34. Stockschlaeder, M.; Schneppenheim, R.; Budde, U. Update on von Willebrand Factor Multimers: Focus on High-Molecular-Weight Multimers and Their Role in Hemostasis. *Blood Coagul Fibrinolysis* **2014**, *25*, 206–216, doi:10.1097/MBC.0000000000000065.
35. Springer, T.A. Von Willebrand Factor, Jedi Knight of the Bloodstream. *Blood, The Journal of the American Society of Hematology* **2014**, *124*, 1412–1425.
36. Fowler, W.E.; Fretto, L.J.; Hamilton, K.K.; Erickson, H.P.; McKee, P.A. Substructure of Human von Willebrand Factor. *The Journal of clinical investigation* **1985**, *76*, 1491–1500.
37. Singh, I.; Shankaran, H.; Beauharnois, M.E.; Xiao, Z.; Alexandridis, P.; Neelamegham, S. Solution Structure of Human von Willebrand Factor Studied Using Small Angle Neutron Scattering. *J. Biol. Chem.* **2006**, *281*, 38266–38275, doi:10.1074/jbc.M607123200.
38. Slayter, H.; Loscalzo, J.; Bockenstedt, P.; Handin, R.I. Native Conformation of Human von Willebrand Protein. Analysis by Electron Microscopy and Quasi-Elastic Light Scattering. *J. Biol. Chem.* **1985**, *260*, 8559–8563.
39. Fu, H., Jiang, Y., Yang, D., Scheiflinger, F., Wong, W. P., & Springer, T. A. (2017). Flow-Induced Elongation of von Willebrand Factor Precedes Tension-Dependent Activation. Nature Communications, 8(1), 1-12.
40. Steppich, D.M.; Angerer, J.I.; Sritharan, K.; Schneider, S.W.; Thalhammer, S.; Wixforth, A.; Alexander-Katz, A.; Schneider, M.F. Relaxation of Ultralarge VWF Bundles in a Microfluidic–AFM Hybrid Reactor. *Biochemical and Biophysical Research Communications* **2008**, *369*, 507–512, doi:10.1016/j.bbrc.2008.02.062.
41. Pope, S.B. Turbulent Flows. *Meas. Sci. Technol.* **2001**, *12*, 2020, doi:10.1088/0957-0233/12/11/705.
42. Lippok, S.; Radtke, M.; Obser, T.; Kleemeier, L.; Schneppenheim, R.; Budde, U.; Netz, R.R.; Rädler, J.O. Shear-Induced Unfolding and Enzymatic Cleavage of Full-Length VWF Multimers. *Biophysical Journal* **2016**, *110*, 545–554, doi:10.1016/j.bpj.2015.12.023.
43. Jhun, C.-S.; Reibson, J.D.; Cysyk, J.P. Effective Ventricular Unloading by Left Ventricular Assist Device Varies with Stage of Heart Failure: Cardiac Simulator Study. *Asaio Journal* **2011**, *57*, 407–413.
44. Morabito, M.; Dong, C.; Wei, W.; Cheng, X.; Zhang, X.F.; Oztekin, A.; Webb, E. Internal Tensile Force and A2 Domain Unfolding of von Willebrand Factor Multimers in Shear Flow. *Biophysical Journal* **2018**, *115*, 1860–1871, doi:10.1016/j.bpj.2018.09.001.
45. Ying, J.; Ling, Y.; Westfield, L.A.; Sadler, J.E.; Shao, J.-Y. Unfolding the A2 Domain of Von Willebrand Factor with the Optical Trap. *Biophysical Journal* **2010**, *98*, 1685–1693, doi:10.1016/j.bpj.2009.12.4324.

46. Zhang, X.; Halvorsen, K.; Zhang, C.-Z.; Wong, W.P.; Springer, T.A. Mechanoenzymatic Cleavage of the Ultralarge Vascular Protein von Willebrand Factor. *Science* **2009**, *324*, 1330–1334, doi:10.1126/science.1170905.
47. Li, Z.; Lin, J.; Sulchek, T.; Cruz, M.A.; Wu, J.; Dong, J.; Zhu, C. Domain-Specific Mechanical Modulation of VWF–ADAMTS13 Interaction. *MBoC* **2019**, *30*, 1920–1929, doi:10.1091/mbc.E19-01-0021.
48. Morshed, K.N.; Jr, D.B.; Forleo, M.; Dasi, L.P. Theory to Predict Shear Stress on Cells in Turbulent Blood Flow. *PLOS ONE* **2014**, *9*, e105357, doi:10.1371/journal.pone.0105357.

CHAPTER 4: TUBULAR HEART ASSISTANT PUMP

4.1 INTRODUCTION

Although mechanical circulatory support saved many lives during the last decade, clinical observations have shown that the continuous flow pumps are associated with a much higher incidence of gastrointestinal bleeding, kidney problems, among others, compared with the earlier generation pulsatile pumps [10-16]. However, the presence of several moving mechanical components made the pulsatile pumps less durable, bulky and prone to malfunction, ultimately leading to favor toward continuous flow designs [1-8]. In an attempt to take the best features of both pump types, we designed an experimental study to test a tubular pulsatile pump and find the best timing. Flow and pressure were measured relative to a failing heart simulator. The effect of counter-pulsation and the systolic time were quantified. Heart assist tube (HAT) is providing sufficient flowrate (10 L/min) and pressure (120mmHg), working in counter-pulsation mode and systolic time of 0.3-0.4T. Heart assist tube provided maximal flow pulsatility and an adequate pressure which makes it appropriate for use as paracorporeal or VAD upon further design.

4.2 METHOD

4.2.1 EXPERIMENTAL METHOD

The prototype heart assist tube (HAT) is created to purely test potential pulsatile hemodynamics relative to a failing heart. The prototype HAT operates as a bulb pump, consisting of a flexible inner tube integrated inside a rigid tube that houses a one-way check valve at each end. Air pressure is controlled between the flexible and rigid tube to control contraction or expansion of the flexible tube to drive fluid volume displacement (Fig. 4.1). The rigid tube is transparent thick walled flexible polyvinyl chloride (PVC). The inner tube is a flexible butyl rubber (Fig.4.1c). A control system involving an Arduino is used to switch between the positive and negative air pressure, through the control of solenoid valves. Solenoid valves open and close the positive pressure and negative pressure supply hoses to inflate and deflate the inner tube.

To test HAT pulsation in relation to failing heart simulator, a flow loop test fixture was created through PVC, using a similar design to the Georgia Tech Left Heart Simulator (LHS) that has been used to study heart valves [17]. The flow loop consists of a compliance chamber and adjacent ball valve to mimic systemic circulation hydraulic compliance and resistance. The flow loop also contains a LHS bulb pump that replicates the output flow of a failing heart. Ball valves are placed in the flow loop to direct flow. Specifically, to setup the failing heart, A, B and D valves are closed, C valves is opened. To simulate the HAT attached to the atrium, except B valve all the other valves are open. To simulate the HAT attached to the ventricle, valve A is closed, and valve B is open.

Pressure transducers (P55 Validyne engineering, Northridge, California, USA) measure the pressure drop across the heart tube prototype and across the heart mimic. A flow sensor (ME 20 PXL- Transonic, Davis, California, USA) is used to measure the output flow rate of the HAT prototype and LHS. The flow probe and pressure transducers are connected to a data acquisition (DAQ) system (National instrument, Austin, Texas, USA). The DAQ is monitored on a computer, where Labview (National Instruments, Austin, Texas, USA) is used to control the pneumatic system. Arduino, open source microcontroller, controls the solenoid valves to enable air and vacuum. The Arduino code was altered to study the effect of phase shift between the HAT and the LHS. The effect of the systolic time is also applied by defining the opening and closing intervals of the solenoids by Arduino. Water is used as the working fluid. Water, compared to a more accurate blood analogue, is safe, inexpensive, easy to clean and readily available. However, the Reynolds number will be higher than it would be if a blood analogue were used [18].

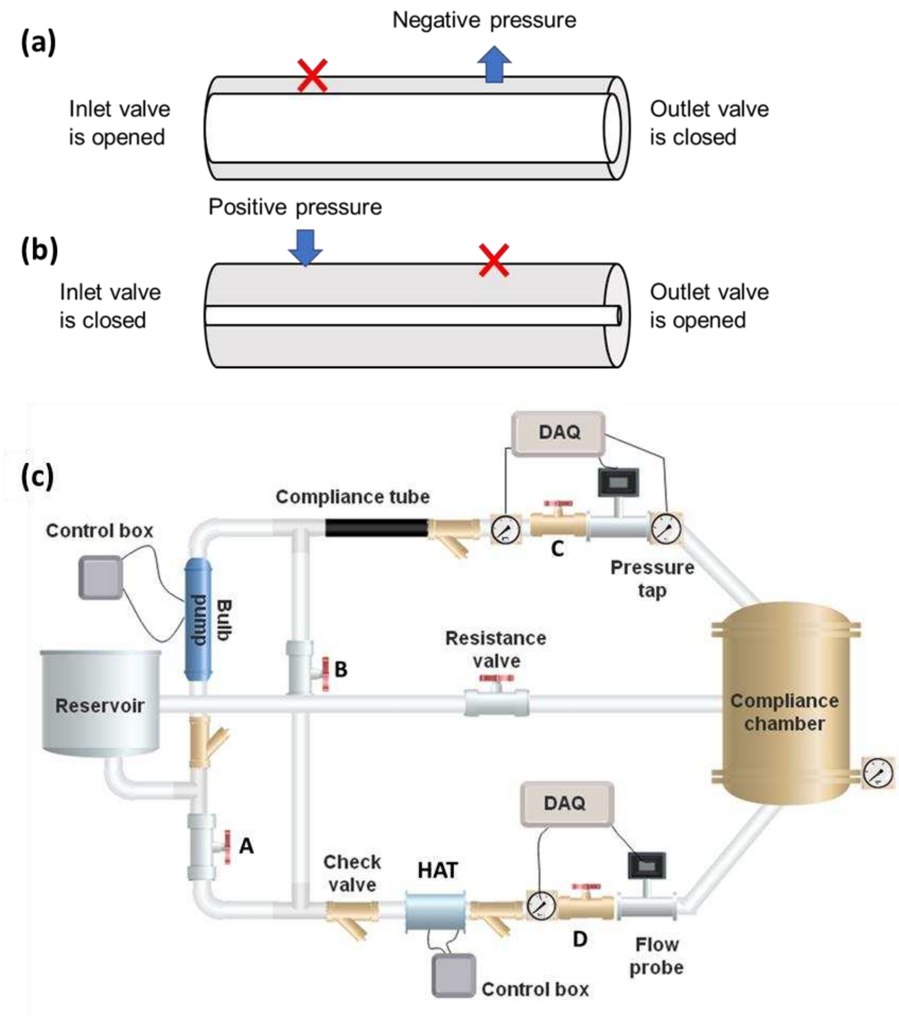

Figure 4.1: Experimental setup and the heart assist tube (HAT) drawing. (a) HAT working principle in diastole (b) HAT working principle in systole (c) Flow loop parts, Bulb pump is the left heart simulator (LHS). DAQ is data Acquisition, control box is for controlling the timing of the negative and positive pressure, resistance valve is for applying resistance to the flow, flow probe is providing the flowrate data and pressure tap is for measuring the flow pressure. Several valves, named A-D are used to simulate different attachment configurations.

4.2.2 SIMULATION METHOD

The 2D axisymmetric simulations were conducted as for the pump with some modifications. The fluid in the pump was assumed to be incompressible and Newtonian. Numerical simulations and mesh generation were performed with ANSYS 18.1 (Pittsburgh, Pennsylvania, U.S.A.). A mesh sensitivity analysis was carried out to ensure that the numerical solutions are mesh independent with tetrahedral elements totaling 500,000 elements. The moving boundary condition at the inlet is set to velocity equal to zero as we are simulating the pump in systolic phase and the pressure at the outlet is set to a lumped model. The moving wall has the contracting speed equal to the experiment.

4.3 RESULTS

Normal left ventricular function is simulated by adjusting the LHS resistance, compliance, and timing, with a representative flow output given Fig.4.2a. Once adjusted, an average and maximum flow rate of 5.5 and 24 L/min can be achieved for a diastolic and systolic pressure 78 and 129 mmHg. The initial conditions are used to create a baseline healthy heart simulation. However, to mimic a failing heart the ejection fraction is reduced to 20% by reducing the pressure in the LHS bulb pump. In this way, the systemic compliance and resistance remain the same. However, the ‘contractility’ of the LHS is reduced. Upon reducing the pressure supply, a representative output shown in Fig.4.2b can be obtained with an ejection fraction of 16%, where the average and maximum flow rate is 1.08 and 7.17 L/min respectively with a diastolic and systolic pressure of 47 and 64 mmHg. The relatively high frequency oscillations in the flow waveforms are typical of waveforms obtained from mechanical valves in the LHS. The simulated failing heart can be categorized as a NYHA class 4, which would require a VAD [19].

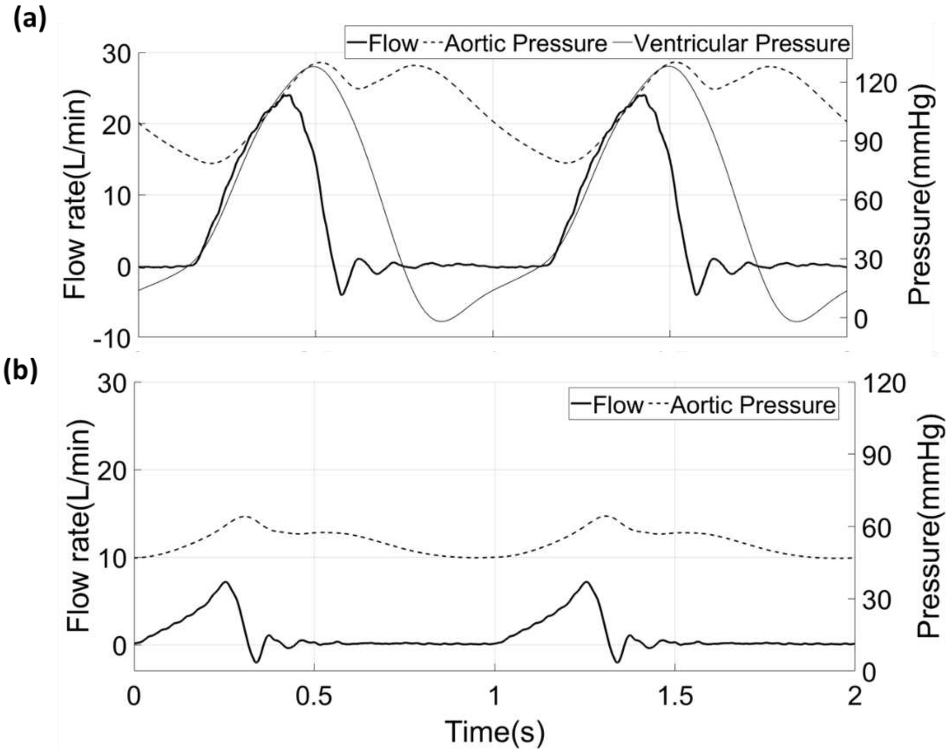

Figure 4.2: The flow rate, aortic pressure, and ventricular pressure from the LHS for (a) healthy and (b) failing heart. T is one period of a cardiac cycle. Results are averaged over 6 cardiac cycle and shown for two periods. Curves are representative.

To test the impact of the HAT on the failing LHS, the HAT was attached to the simulated ventricle with initial conditions involving in-phase pumping with a systolic time of 0.3T, where T is the period of a cardiac cycle. Fig. 4.3a demonstrates how the flow rate and pressure change with these conditions, with the average flowrate increasing 4.4 times to 4.8 L/min, and the maximum flowrate increasing from 7.17 L/min to 37.17 L/min, overall leading to a steeper flow rate curve when compared to the simulated healthy left ventricle from Fig.4.2a. Systolic pressure reaches 110 mmHg, which is a 183% of the FH. The diastolic pressure is also increased from 46.78 mmHg to 56.58 mmHg. In the failing heart, the ventricular pressure remained elevated.

However, the HAT can still increase the failing heart pressure $\left(P_{distaole} = 60mmHg, P_{systole} = 110\ mmHg\right)$ and flow rate $\left(\bar{Q} = 4.8\frac{L}{min}, Q_{maximum} = 44\frac{L}{min}\right)$ into the simulated aorta, Fig. 4.3b. Note that the maximum flow rate is higher for atrial attachment, despite similar cardiac outputs when compared to the healthy ventricle or the ventricle-connected HAT. The simulated aortic systolic pressure is 1.8 times larger than the failing LHS aortic pressure. Overall, the peak and mean flow and aortic pressure are similar regardless of HAT attachment point, but the ventricle remains loaded with an elevated pressure when the HAT is attached to the atrium.

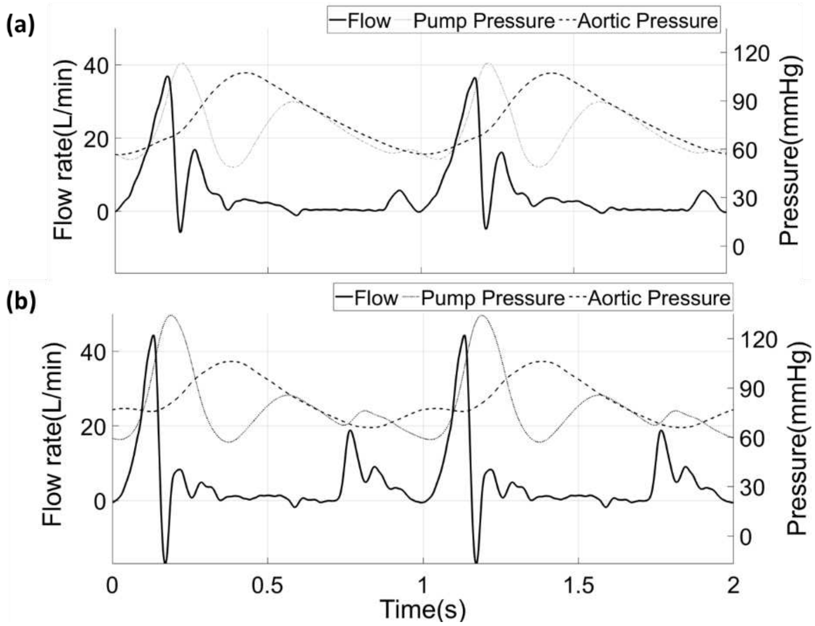

Figure 4.3. Pressure and flow rate of the failing heart assisted with the heart assist tube (a) when the HAT is connected ventricle (b) when the HAT is connected to the atrium. There is no phase difference between the failing heart and the HAT. The systolic time is 0.3s and the heart rate is 60 beat per minute heart rate.

The advantage of co-pulsation and counter-pulsation has been studied. To investigate pulsation timing, the phase difference between the FH and the HAT was adjusted between 0 and 2π. The baseline FH pressure and flowrate are designated as the P_{base} and Q_{base}. Other than phase shift, all other parameters of the LHS and HAT are held constant.

Attaching the HAT to the ventricle, decreases the FH average flowrate by 50%. However, the ideal situation is having the FH pump minimally, and the aortic valve keeps working[20]. It is necessary to have the ability of increasing the FH pumping function and giving the option to the technicians to increase the FH flowrate by adjusting the HAT pumping contractility based on the patient needs[20,21].

To maintain close to 50% of flow out of the aortic valve, avoiding increased dysfunction, it is best to avoid co-pulsation when attached to the atrium and counter-pulsation when attached to the ventricle, Fig4.4a. The HAT mean flow rate (attached to the ventricle or atrium) to the base flowrate for different phase shifts are calculated and shown in Fig4.4b. The phase shift 0.4 π -0.9 π gives the largest values of the mean HAT flowrate. The total flow is always larger than the optimal value (shown by green line) except for large phase shifts, connected to the ventricle. To conclude, connecting the HAT to the ventricle maintains the aortic valve function and provides sufficient flow for the phase shifts 0.2-0.6 π, which can lead to normal circulatory function.

The HAT mean pressure (attached to the ventricle or atrium) to the base pressure is shown in Fig 4.4d. The mean atrium pressure is larger when the HAT is attached to the ventricle and out of phase. The largest mean pressure (attached to the ventricle) is for the phase shift 0.4-0.6 π, while the lowest is at the phase shift of 1.6 π. Overall, the mean pressure varied by only 10% as a function of phase shift. The preferred condition is when the HAT the ability to provide the largest pressure which is when it is attached to the ventricle and works whiting the range of 0.4-0.8 π.

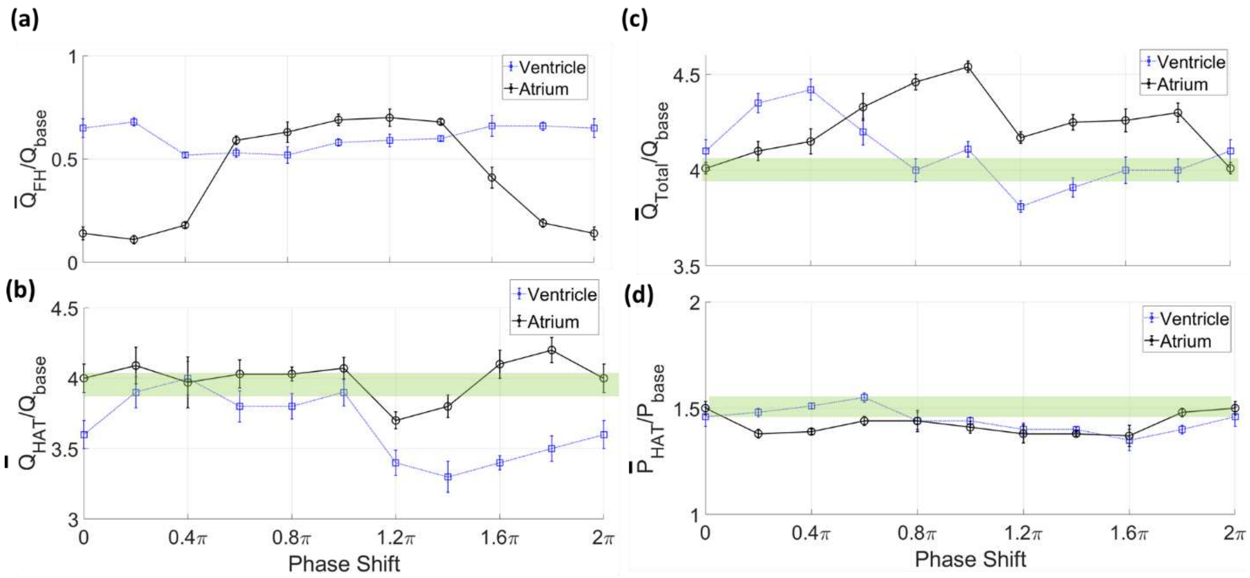

Figure 4.4. The effect of phase shift when the HAT is connected to the ventricle and atrium for (a) failing heart mean flowrate to the base flow rate, (b) HAT mean flowrate to the base flow (c) total flowrate to the base flow, (d) HAT mean pressure to the base pressure. π is completely out of phase and 0 is in phase. The FH pressure and flowrate with no assistance is called the base pressure and the base flow rate. The physiological value for a healthy adult heart is shown in green.

The systolic time can affect fluid inertia, which can lead to changes in pressure and flow patterns in the system. The effect of varying the systolic time from 0.1-0.5(s) on flowrate and pressure (with no phase difference) is shown in Fig.4.5. The mean FH and HAT flow rate for different systolic time when the HAT is connected to the ventricle and atrium is shown in Fig. 4.5a. Increasing the systolic time increases the FH mean flowrate when the HAT is connected to the ventricle. When the HAT is connected to the atrium, the mean and total flowrates are falling by increasing the systolic time. The HAT flow rate is increasing for larger systolic time (Fig.4. 5b). The total flowrate is close to the physiological values for the systolic time of 0.2-0.5s. The mean HAT and FH pressure for different systolic time when the HAT is connected to the ventricle and atrium is shown in Fig. 4.5d. Mean HAT pressure when it is connected to the ventricle is maximum for systolic time 0.4T (Fig. 4.5d). Mean HAT pressure is at the maximum value for systolic time 0.3T when it is connected to the atrium. In conclusion, the systolic time of 0.3T makes the FH working harder. However the systolic time of 0.1T decreases the FH working load.

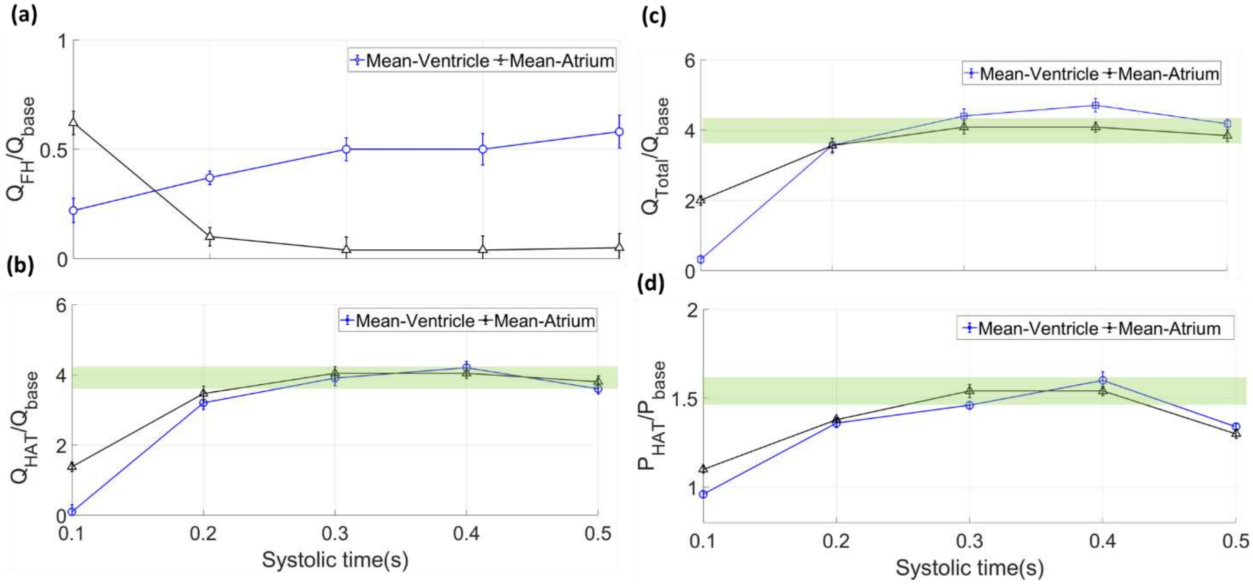

Figure 4.5. The effect of systolic time of the HAT on the flow rate and pressure when HAT is connected to atrium and ventricle (a) FH mean flow rate to the base flowrate (b) HAT mean flow rate to the base flowrate (c) Total mean flowrate to the base pressure (d) HAT mean pressure to the base pressure . The FH pressure and flowrate with no assistance are called the base pressure and the base flow rate respectively.

To find the effect of the attachment configuration and phase shift on the FH working load, we have calculated the work done by the FH, shown in Fig. 4.6. The work done by the FH without assistance has been identified as W_{base}. By comparing the W_{base} with the work done by FH being attached, the best attachment configuration is identified. When the HAT is connected to the ventricle, the work done by the FH is close to 100% for phase shifts 1.4π- 2π. This work is equal to the work done by the FH working without assist. Out of phase (0.8 π-1.2 π) condition dropped the work to less than 50%. The work done by the FH is close zero when the HAT is connected to the atrium with the phase shift 0 and 0.2π. The effect of HAT systolic time on the work done by the failing heart with no phase shift is shown in Fig.6b. The work done by the FH without assistance has been identified as base work. Increasing the systolic time, increases the FH work when the HAT is attached to the ventricle. In conclusion, the work done by the FH is minimum and not zero when the HAT is either attached to the ventricleor atrium with the phase shift 0.8-1.2 π. Moreover, Increasing the systolic time decreases the FH work to almost zero when it is attached to the atrium.

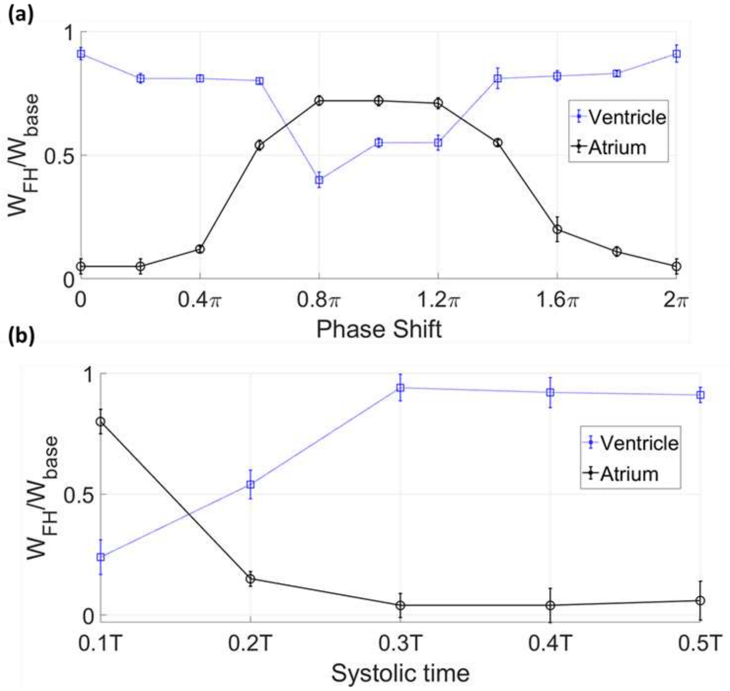

Figure 4.6. The effect of the (a) phase shift and (b) systolic time on the work done by the FH to the base work. The base work is the work done by the FH with no assistant.

To find the shear rate and turbulent flow intensity in the pump, we have used the simulation results. Based on Fig. 4.7, the shear rate doesn't exceed 400 1/s and the Reynolds number is equal to 1500. Therefore, we don't expect to have turbulent flow and consequently medical complications.

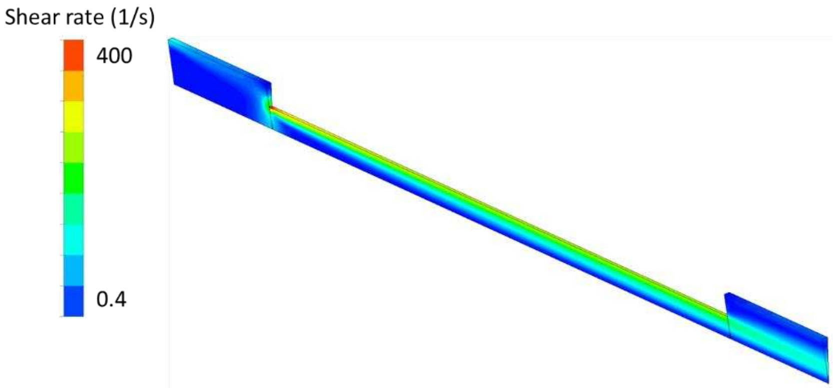

Figure 4.7. Simulation results in the pump during the systole. The dimensions are based on the HAT used in the experiment.

The three different criteria such as normal circulation, reducing the load on the ventricle and aortic function for each configuration are listed in table 4.1. Normal circulation configuration is chosen based on having the sufficient biological pressure and flowrate. The load on the ventricle is defined by the FH work done in different configurations. To keep the aortic valve working after the HAT attachment, it is necessary to have the fluid flow through the valve. All these 3 concepts have been discussed in this study. However, to find the optimum condition, we have summarized all the optimum values in table.4.1. The overall optimum phase shift and systolic time are not defined as we have not found a range which all the criteria are satisfied. When the HAT is connected to the ventricle the optimum range is 0.8π to 1.2π for the phase shift. For the systolic time, it should be adjustable to switch between 0.1T to 0.4T based on the patient condition.

Table 4.1. The optimum working condition of the HAT. Not defined (ND) is used when there is no range to satisfy all the criteria.

	Phase change		Systolic time	
Attached to	atrium	ventricle	atrium	ventricle
Maximum circulatory function	0 and 1.8 π	0.4π to 0.8π	0.3T to 0.4T	0.3T to 0.4T

Minimum Ventricle load	0.4π to 0.6π & 1.4π to 1.8π	0.8-1.2 π	0.2T	0.1T
Aortic valve functioning	0.8π to 1.4π	0 to 2 π	0.1T to 0.2T	0.3T to 0.4T
Optimum	ND	0.8π to 1.2π	ND	ND

We were able to recapitulate flow and pressure waveforms in our LHS with that of a healthy human heart. To study how hemodynamics are affected by a HAT, we also simulated a failing heart by reducing contractility. Flow and pressure waveforms were able to be recovered with the application of the HAT. This work demonstrates that a tubular pump can function as a VAD with minimal tribological wear sources that otherwise plagued prior pulsatile VADs. Results can be extended for choosing pulsatile conditions in other pumps.

Attaching the HAT to the atrium or ventricle has an effect of flow and pressure. Although the peak flow rate is larger when the HAT is connected to the atrium, the average flow rate is the same regardless of connecting the HAT to the ventricle or atrium (no phase difference). This is related to the large amount of back flow in the HAT while its connected to the atrium (Fig. 4.3, 4). The aortic pressure and the HAT pressure are in the same range (60-110 mmHg) during the systole and diastole when the HAT is connected to the ventricle. The ventricular pressure is not reaching to the aortic pressure in the FH when the HAT is connected to the atrium which is the reason of not having flow out of the aortic valve (Fig. 4.3b, 4). Aortic valve abnormalities can develop due to bypassing the valve [22]. Therefore, attaching the HAT to the ventricle helps the aortic valve functioning.

The phase shift can change the flow and pressure. The average flow rate is larger when the HAT is connected to the ventricle and is working within the phase shifts of 0.2-0.8 π. Several previous studies showed that counter-pulsation control of the pulsatile LVAD can reduce severe cardiac load variations and stabilize the blood pumping of the native heart [23,24]. The FH is able to pump when the ventricular systolic pressure becomes equal or larger than the aortic pressure LHS can't overcome that aortic pressure when pumping in phase. Consequently, there is less resistance for the FH to pump – the HAT and LHS aren't increasing aortic pressure at the same time (Fig.4.4). However, when the HAT is connected to the ventricle, if the phase shift is in the range of 0.8 π to 1.2 π, HAT pull fluid from the ventricle, providing less preload when the ventricle is ready to pump (Fig.4.4). Overall, that VADs pumping from the atrium would not work well with co-pulsation, but instead require counter-pulsation. However, for VADs connected to the ventricle can handle any phase, while operating with the highest peak flow rate for counter-pulsation.

Changing the systolic time is changing the contraction of the HAT which affect fluid momentum and inertia; this affects the aortic pressure. The largest flow rate and pressure is related to the systolic time 0.3T and 0.4T. For any systolic time, smaller than 0.3T, the dynamics of the inner tube of the HAT can't keep up, therefore it cannot provide the enough flow and pressure (Fig.4.5). Increasing the systolic time to 0.5T also has a negative effect of the produced flow and pressure as the diastolic time decreases and the inner tube cannot fully expand (Fig.4.5). Therefore, the systolic time of 0.3T-0.4T is the optimum systolic time regardless of attachment configuration.

The work done by the failing heart with no assist is smaller than the healthy heart as it has smaller stroke volume and aortic pressure (Fig.4.6). Comparing the FH work that receives assistance from the HAT to without assistance, it is necessary to find the best working condition. If the FH works less than a failed heart, it can cause the heart muscle degradation and pressuring the heart to work harder also can worsen the heart failure[25].

The second wave in flow caused by the second wave in HAT pressure is happening in the flow loop may not exist in a human. This in vitro study has several simplifications and limitations. The mock circulatory system was an idealized model of the cardiovascular system. The rigidity of the system and adding some compliance components might results in non-physiologic augmentation of pulse pressure. In addition, the mechanical check valves that used are not the best alternative for the heart valves. Some of the vibration in the system are related to these valves.

This approach provided maximal flow plasticity and an adequate pressure, which may be elevated in recipients of a cardiac replacement device. Further bench and in vivo experiments are needed to assess pump durability and functionality in different conditions. Moreover. the device needs to be made of biocompatible materials and tested with prosthetic heart valves.

4.4 REFERENCES

1. Englert, J.A.; Davis, J.A.; Krim, S.R. Mechanical Circulatory Support for the Failing Heart: Continuous-Flow Left Ventricular Assist Devices. *Ochsner Journal* **2016**, *16*, 263–269.
2. Reddy, K.S. Global Perspective on Cardiovascular Disease. *Evidence-Based Cardiology* **2003**, *91102*.
3. Ziaeian, B.; Fonarow, G.C. Epidemiology and Aetiology of Heart Failure. *Nature Reviews Cardiology* **2016**, *13*, 368–378.
4. Inamdar, A.A.; Inamdar, A.C. Heart Failure: Diagnosis, Management and Utilization. *Journal of clinical medicine* **2016**, *5*, 62.
5. Caraballo, C.; Desai, N.R.; Mulder, H.; Alhanti, B.; Wilson, F.P.; Fiuzat, M.; Felker, G.M.; Piña, I.L.; O'Connor, C.M.; Lindenfeld, J. Clinical Implications of the New York Heart Association Classification. *Journal of the American Heart Association* **2019**, *8*, e014240.
6. Lund, L.H.; Matthews, J.; Aaronson, K. Patient Selection for Left Ventricular Assist Devices. *European journal of heart failure* **2010**, *12*, 434–443.
7. Bhat, G.; Gopalakrishnan, M.; Aggarwal, A. Gastrointestinal Bleeding with Continuous Flow Left Ventricular Assist Devices (LVADs). *Recent Advances in the Field of Ventricular Assist Devices* **2013**, doi:10.5772/56010.
8. Flaherty, M.P.; Moses, J.W.; Westenfeld, R.; Palacios, I.; O'Neill, W.W.; Schreiber, T.L.; Lim, M.J.; Kaki, A.; Ghiu, I.; Mehran, R. Impella Support and Acute Kidney Injury during High-Risk Percutaneous Coronary Intervention: The Global CVAD Renal Protection Study. *Catheterization and Cardiovascular Interventions* **2020**, *95*, 1111–1121.
9. Kannel, W.B. Hazards, Risks, and Threats of Heart Disease from the Early Stages to Symptomatic Coronary Heart Disease and Cardiac Failure. *Cardiovascular drugs and therapy* **1997**, *11*, 199–212.
10. Prinzing, A.; Herold, U.; Berkefeld, A.; Krane, M.; Lange, R.; Voss, B. Left Ventricular Assist Devices—Current State and Perspectives. *J Thorac Dis* **2016**, *8*, E660–E666, doi:10.21037/jtd.2016.07.13.
11. The Past, Present and Future of the Device Keeping Alive Carew, Thousands of HF Patients Available online: https://www.heart.org/en/news/2018/06/13/the-past-present-and-future-of-the-device-keeping-alive-carew-thousands-of-hf-patients (accessed on 29 May 2020).
12. Chair, S.Y.; Yu, D.S.; Ng, M.T.; Wang, Q.; Cheng, H.Y.; Wong, E.M.; Sit, J.W. Evolvement of Left Ventricular Assist Device: The Implications on Heart Failure Management. *J Geriatr Cardiol* **2016**, *13*, 425–430, doi:10.11909/j.issn.1671-5411.2016.05.015.
13. Rodriguez, L.E.; Suarez, E.E.; Loebe, M.; Bruckner, B.A. Ventricular Assist Devices (VAD) Therapy: New Technology, New Hope? *Methodist Debakey Cardiovasc J* **2013**, *9*, 32–37.
14. Prinzing, A.; Herold, U.; Berkefeld, A.; Krane, M.; Lange, R.; Voss, B. Left Ventricular Assist Devices—Current State and Perspectives. *Journal of thoracic disease* **2016**, *8*, E660.
15. Banfi, C.; Rigamonti, F.; Ahmadov, K.; Meyer, P.; Hachulla, A.-L.; Craviari, C.; Fontana, P.; Bendjelid, K.; Giraud, R. An Unusual Thrombus Location in a Heartmate 3TM Device with Fatal Outcome. *Perfusion* **2019**, 0267659119890218.
16. Ootaki, C.; Yamashita, M.; Ootaki, Y.; Kamohara, K.; Weber, S.; Klatte, R.S.; Smith, W.A.; Massiello, A.L.; Emancipator, S.N.; Golding, L.A. Reduced Pulsatility Induces

Periarteritis in Kidney: Role of the Local Renin–Angiotensin System. *The Journal of thoracic and cardiovascular surgery* **2008**, *136*, 150–158.

17. Bark, D.L.; Vahabi, H.; Bui, H.; Movafaghi, S.; Moore, B.; Kota, A.K.; Popat, K.; Dasi, L.P. Hemodynamic Performance and Thrombogenic Properties of a Superhydrophobic Bileaflet Mechanical Heart Valve. *Annals of biomedical engineering* **2017**, *45*, 452–463.
18. Midha, P.A.; Raghav, V.; Okafor, I.; Yoganathan, A.P. The Effect of Valve-in-Valve Implantation Height on Sinus Flow. *Ann Biomed Eng* **2017**, *45*, 405–412, doi:10.1007/s10439-016-1642-2.
19. Hajouli, S.; Ludhwani, D. Heart Failure And Ejection Fraction. **2020**.
20. Topilsky Yan; Hasin Tal; Oh Jae K.; Borgeson Daniel D.; Boilson Barry A.; Schirger John A.; Clavell Alfredo L.; Frantz Robert P.; Tsutsui Rayji; Liu Mingya; et al. Echocardiographic Variables After Left Ventricular Assist Device Implantation Associated With Adverse Outcome. *Circulation: Cardiovascular Imaging* **2011**, *4*, 648–661, doi:10.1161/CIRCIMAGING.111.965335.
21. Dandel Michael; Weng Yuguo; Siniawski Henryk; Potapov Evgenij; Drews Thorsten; Lehmkuhl Hans B.; Knosalla Christoph; Hetzer Roland Prediction of Cardiac Stability After Weaning From Left Ventricular Assist Devices in Patients With Idiopathic Dilated Cardiomyopathy. *Circulation* **2008**, *118*, S94–S105, doi:10.1161/CIRCULATIONAHA.107.755983.
22. John, R.; Mantz, K.; Eckman, P.; Rose, A.; May-Newman, K. Aortic Valve Pathophysiology during Left Ventricular Assist Device Support. *The Journal of heart and lung transplantation* **2010**, *29*, 1321–1329.
23. Choi, S.W.; Nam, K.W.; Lim, K.M.; Shim, E.B.; Won, Y.S.; Woo, H.M.; Kwak, H.H.; Noh, M.R.; Kim, I.Y.; Park, S.M. Effect of Counter-Pulsation Control of a Pulsatile Left Ventricular Assist Device on Working Load Variations of the Native Heart. *Biomedical engineering online* **2014**, *13*, 35.
24. Wang, Y.; Koenig, S.C.; Sobieski, M.A.; Slaughter, M.S.; Giridharan, G.A. Hemodynamic Benefits of Counterpulsation, Implantable, Percutaneous, and Intraaortic Rotary Blood Pumps: An In-Silico and In Vitro Study. *Cardiovascular Engineering and Technology* **2017**, *8*, 439–452.
25. Burke, M.A.; Givertz, M.M. Assessment and Management of Heart Failure after Left Ventricular Assist Device Implantation. *Circulation* **2014**, *129*, 1161–1166.

CHAPTER 5: CONCLUSION AND FUTURE DIRECTIONS

Based on chapter 1, the bleeding disorders, lack of pulsation, and infection are some of the main reasons of medical complications in VAD patients. Some of these issues can be solved by finding an alternative method of pumping blood than using continuous flow pumps. One solution is using a pumping mechanism in early stages of the heart development as it is efficient and less complicated than an adult heart. Therefore, in chapter 2 we have developed a computational multiphysics model to study the interplay between mechanical properties, pumping mechanism, and blood flow in the embryonic zebrafish heart. Our results show that the tubular heart contraction can provide sufficient pulsatile flow. Therefore, scaling up the zebrafish embryonic heart to a tubular heart assist device is a potential solution. However, the tubular heart assist device is not capable of providing large pressure values without valves. To solve this issue, valves at the inlet and outlet of the tubular pump is necessary to achieve the biological systolic pressure of a healthy heart.

The other common complication is the bleeding disorders in the LVAD patients. Most of the previous studies related the bleeding disorders to high shear rate in laminar flow. However, our results in chapter 3 suggests that the bleeding disorders are highly related to the turbulent flow and VWF interactions with turbulent flow forces. We also used polymer science theories to understand the VWF breakage quantitively in laminar and turbulent flow. These data show the importance of having the heart assist device free from turbulent flow.

After building the heart assist tube, the output in the form of flow and pressure were measured relative to a failing heart simulator in chapter 4. The effect of counter-pulsation and the systolic time were quantified. The heart assist tube provides a sufficient flowrate (10 L/min) and pressure (120mmHg), working in counter-pulsation mode and systolic time of 0.3-0.4T. The heart assist tube provided maximal flow pulsatility and an adequate pressure which makes it appropriate for use as paracorporeal or VAD upon further design.

Further bench and in vivo experiments are needed to assess pump durability and functionality in different conditions. Moreover. the device needs to be made of biocompatible materials and tested with prosthetic heart valves. The polymeric heart valves must be accurately sized, built and integrated inside the heart tube. Heart valves need to be tested in the flow loop to make sure they are working properly. The effective orifice area, valve leaflet motion, pressure drop and flow behavior across the valve needs to be studied. The size of the tubular pump needs to be adjusted to the outflow graft. As the outflow graft is not large enough to have an equal size to the left ventricle, a housing with the dimensions of heartmate 3 pump should be added to the outflow graft. Moreover, to eliminate the driveline infection, the whole device needs to be fully implantable. This is achievable by using the tubular heart assist device if the actuating mechanism can be triggered externally.